Universitat Autònoma de Barcelona

Optimisation of CSD buffer layers for $YBa_2Cu_3O_7$ coated conductor development

Andrea Cavallaro

Director
Dr. Felip Sandiumenge

Codirector
Prof. Xavier Obradors

Tutor
Prof. Jaume Casabó

Bellaterra, 6 juny 2005

ACKNOWLEDGMENTS

My acknowledges to Dr.Felip Sandiumenge, supervisor of my Thesis, and Professor Xavier Obradors from the Institut de Ciència de Materials de Barcelona-CSIC, for the opportunity to participate to the European project called SOLSULET.

To Professor Jaume Casabó, tutor of my Thesis.

To the MARIE CURIE COMMUNITY, the SOLSULET project, and the LA FARGA for the financial support.

To Dr. Teresa Puig, Dr, Salva Piñol and Dr. Narcis Mestres for their scientific support.

To Professor H. C. Freyhardt from Göttingen University in Germany and J.Evetts from Cambridge University for supplying the metal technical substrates.

To Dr. Pep Bassa for its support on using the XRD texture four-circle Goniometer Philips PW 3710 mpd control at the "Serveis cientifico Tècnics" of Barcelona University.

To Dr.Anna Palau, Dr.Alberto Pomar and Mr. Joffre Gutierrez for the SQUID and resistivity measurements.

To Jaume Gazquez for the TEM analysis of ceria samples, fundamental at the time of interpreting the films growth.

To Dr.Laura Fernandez and Mr. Joffre Gutierrez for PLD-YBCO deposition on CSD tamplates.

To Mr. J. Esquius and Mr. J.Campos for XRD measurements.

To Dr. Judit Orò for the TGA analysis, to Miss Ana Esther Carrillo for the SEM ones, Miss. Maria Jesus and Dr. Angel Pérez for the AFM measurements, Ms. Anna Fernández for the H-NMR analysis.

To Mr. Toni Pons, Mr. Josep Roig, Mr. Oriol Sabater and Mr. Jose Rodríguez for technical support.

CONTENTS

CONTENTS i

ABBREVIATED TERMS iv

APPENDIX 1 vii

1 INTRODUCTION 1

1.1 SUPERCONDUCTING MATERIALS 1
1.1.1 AN HISTORICAL OVERVIEW 2
1.2 SUPERCONDUCTING PROPERTIES 3
1.2.1 PENETRATION DEPTH (λ) AND COHERENCE LENGTH (ξ) 4
1.2.2 TYPE I AND TYPE II SUPERCONDUCTORS 5
1.2.3 IRREVERSIBILITY CURVE 6
1.3 CONTEXT OF THE PRESENT RESEARCH 7
1.4 $YBa_2Cu_3O_7$ SUPERCONDUCTING COATED CONDUCTOR 9
1.5 SOL-GEL ROUTE 12
1.5.1 OVERVIEW OF THE CHEMICAL SOLUTION DEPOSITION (CSD) PROCESSES 13
1.5.2 DEPOSITION PROCESSING 17
1.5.3 THERMAL CRYSTALLIZATION 20
1.5.4 CRYSTAL GROWTH (THERMODYNAMIC AND KINETIC MODELS) 21
1.5.5 HIGHLY TEXTURED FILMS BY CSD 29

1.6 EXPERIMENTAL TECHNIQUES 30
1.6.1 X-RAY DIFFRACTION 30
1.6.2 SMALL ANGLE X-RAY REFLECTIVITY(XRR) 32
1.6.3 SECONDARY ELECTRON MICROSCOPY (SEM) 33
1.6.4 X-RAY PHOTOELECTRON SPECTROSCOPY (XPS) 34
1.6.5 REFLECTION HIGH ENERGY ELECTRON DIFFRACTION (RHEEED) 34
1.6.6 ATOMIC FORCE MICROSCOPY (AFM) 35
1.6.7 INFRA RED MICROSCOPY (IR) 36
1.6.8 INTERFEROMETRY 37

2 IMPORTANCE OF THE STUDY OF CSD BUFFER LAYERS FOR THE OPTIMISATION OF COATED CONDUCTOR ARCHITECTURES 41

2.1 INTRODUCTION 41
2.2 AIMS AND STRATEGY 42

2.3 TECHNICAL METAL SUBSTRATES 43
2.4 THE PROPER BUFFER LAYER ARCHITECTURE 45

3 GROWTH OF CeO_2 BUFFER LAYERS BY MOD 50

3.1 SYNTHESIS AND GROWTH OF CeO_2 FILMS ON (001)-YSZ SINGLE CRYSTALS 50
3.2 PRECURSOR SOLUTIONS AND DEPOSITION PARAMETERS 53
3.2.1 PREPARATION OF PRECURSOR SOLUTIONS 53
3.2.2 VISCOSITY 55
3.2.3 SPIN COATING 58
3.2.4 PYROLYSIS 60
3.2.5 FILM THICKNESS 65
3.2.6 INTERDIFFUSION 67
3.3 FILM STRUCTURE, TEXTURE AND SURFACE MORPHOLOGY 68
3.3.1 ROUGHNESS VS THICKNESS 71
3.3.2 ROUGHNESS VS GROWTH TEMPERATURE 72
3.4 CONCLUSIONS 74

4 GROWTH MODEL FOR MOD-CeO_2 77

4.1 GROWTH IN AN Ar/H_2 ATMOSPHERE 77
4.2 POST ANNEALING IN STATIC AIR ATMOSPHERE 79
4.3 DIRECT GROWTH OF CeO_2 IN STATIC AIR 87
4.4 SURFACE ENERGY AND MORPHOLOGY 96
4.5 GROWTH MODEL FOR MOD-CeO_2 98
4.5.1 IDENTIFICATION OF AN IMPURITY DRIVEN GROWTH INHIBITION MECHANISME IN FILM GROWTH IN A REDUCING CONDITIONS 98
4.5.2 SUMMARY 102
4.6 SELF-ASSEMBLING OF MOD-CeO_2 ISLANDS 103

5 $BaZrO_3$, $SrTiO_3$ AND $SrTiO_3/BaZrO_3$ ARQUITECTURE (BY THE CHELATE PROCESS) 109

5.1 EXPERIMENTAL 109
5.1.1 SOLUTION SYNTHESIS OF BARIUM ZIRCONATE 109
5.1.2 SOLUTION SYNTHESIS OF STRONTIUM TITANATE 110
5.1.3 FILM DEPOSITION AND THERMAL TREATMENT 110
5.2 RESULTS AND DISCUSSION 111
5.2.1 THICKNESS CONTROL 112
5.2.2 ROUGHNESS DEPENDENCE WITH SYNTHESIS TEMPERATURE 114
5.2.3 STRUCTURES CHARACTERIZATION 115
$SrTiO_3/BaZrO_3$ ON YSZ SINGLE CRYSTAL 115
$SrTiO_3/BaZrO_3$ AND $SrTiO_3$ON MgO SINGLE CRYSTAL 117
5.2.4 EXPERIMENTAL REPRODUCIBILITY 119
5.2.5 OXYGEN EFFECT ON $BaZrO_3$ GROWTH 120
5.2.6 SECONDARY GRAIN GROWTH 122
5.3 FILM BIAXIAL TEXTURE 124

5.3.1 BIAXIAL TEXTURE DEPENDENCE WITH THE FILM SYNTHESIS TEMPERATURE 125
5.4 CONCLUSIONS 126

6 DEPOSITION OF OPTIMISED BUFFER LAYERS ON METAL SUBSTRATES 129

6.1 NiO(SOE)/Ni SUBSTRATE 129
6.2 YSZ(IBAD)/SS SUBSTRATES 134
6.2.1 GROWTH OF CeO_2 FILMS ON IBAD-DEPOSITED YSZ (IBAD) TEMPLATES ON STAINLESS –STEEL TAPES 136
6.2.2 CeO_2 GROWTH IN OXYGEN ATMOSPHERE 138
6.2.3 GROWTH OF $SrTiO_3/BaZrO_3$ FILMS ON IBAD-DEPOSITED YSZ TEMPLATES ON STAINLESS-STEEL TAPES 143

7 SYNTHESIS AND GROWTH OF MOD-TFA YBCO 148

7.1 INTRODUCTION 148
7.2 STATE OF THE ART 149
7.3 EXPERIMENTAL 151
7.3.1 SOLUTION PREPARATION AND DEPOSITION 151
7.3.2 PYROLYSIS 152
7.3.3 FIRING PROCESS 154
7.4 RESULTS ON THE OPTIMISED BUFFER LAYERS 158
7.4.1 TFA DEPOSITION OF YBCO ON CeO_2/YSZ^{SC} 158
7.4.2 TFA DEPOSITION OF YBCO ON CeO_2/YSZ(IBAD)/SS 167
7.4.3 TFA DEPOSITION OF YBCO ON $SrTiO_3/BaZrO_3$/MgO 171
7.4.4 TFA DEPOSITION OF YBCO ON $SrTiO_3/BaZrO_3$/NiO(SOE)/Ni 174
7.5 CONCLUSIONS 177

GENERAL CONCLUSIONS 181

ABBREVIATION TERMS

Nomenclature

α_o	Temperature dependent constant
$\Delta\phi$	FWHM of the *in-plane* texture
$\Delta\omega$	FWHM of the *out-of-plane* texture
ΔG_D	Diffusion energy in nucleation and growth
ΔG_S	Surface energy
ΔG_V	Free energy per volume
ε	Lattice mismatch
θ	Wetting angle
θ	Misorientation angle or tilt angle
λ	Superconducting penetration depth
λ	Atomic jump distance
λ	Wavelength of radiation
γ	Anisotropy factor or Resistivity coefficient
γ_f	Film surface energy
γ_i	Interface energy
γ_s	Substrate surface energy
η	Viscosity
ρ	Normal-state resistivity
σ	Residual stress
ξ	Superconducting coherence length
a, b, c	Unit cell parameters
A	Pre-exponential factor
a.u.	Arbitrary units
c	Light velocity
D	Diffusion coefficient
H^*	Irreversibility field
H_c	Critical magnetic field
H_{c1}	Lower critical magnetic field
H_{c2}	Upper critical magnetic field
H_{ext}	External magnetic field
Hum_{Abs}	Absolutely humidity
Hum_{Rel}	Relative humidity
h	Plank's constant
I	Homogenous nucleation rate
I_c	Critical current
J_c	Critical current density
k	Bolzmann's constant
M_{air}	Air density
P-V	Maximum peak-to-valley
$P(H_2O)$	Water vapour partial pressure

$P_{H2O}Sat(T)$	Water partial pressure at temperature
$P(O_2)$	Oxygen partial pressure
Q	Activation energy
RMS or Rms or rms	Root-mean-square-roughness
r^*	Critical radius size
<r>	Average grain radius
T	Temperature
T_c	Superconducting critical temperature
T_m	Melting temperature
$T_{max\ or}\ T_{syn}$	Synthesis temperature
T_{nuc}	Nucleation temperature
t	Time
t	Sample thickness
x	Oxygen content in $YBa_2Cu_3O_{7-x}$
v	velocity
W^*	Energetic barrier

Acronyms and Initials

Acac	Acetylacetonate or β-diketonate
AFM	Atomic force microscopy
BZO	$BaZrO_3$
Bi-2223	Bismuth strontium calcium copper oxide ($Bi_2Sr_2Ca_2Cu_3O_x$)
CC	Coated conductor
CSD	Chemical solution deposition
EELS	Electron energy loss spectroscopy
EDX	Energy-dispersive X-ray diffraction
FFT	Fast fourier transform
FWHM	Full width at half maximum
GB	Grain boundary
G_c	Critical strain-energy release rate
HTc	High critical temperature
HTs	High-temperature superconductor/s
IBAD	Beam assisted deposition
ICMAB	Institut de Ciència de Materials de Barcelona
IR	Infrared spectroscopy
LAO	$LaAlO_3$
MOD	Metal organic deposition
NMR	Nuclear magnetic resonance
PLD	Pulsed laser deposition
P-V	Peak to valley
R	Gas constant
RABiTS	Rolling-Assisted Biaxially Textured Substrate
RHEED	Reflection high energy electron diffraction
SAD	Selected area diffraction
SAMs	Self-assembled monolayers
SC	Single crystal
SEM	Scanning electron microscopy
SIG	Solvent-into-gel

SMES	Superconducting magnetic energy storage
SOE	Self oxidation epitaxy
SOLSULET	Novel sol gel technology for long length superconducting coated tapes
SQUID	Superconducting quantum interference device
STO	$SrTiO_3$
TEM	Transmission electron microscopy
TFA	Trifluoroacetate
TGA	Thermal gravimetric analysis
UAB	Universitat Autònoma de Barcelona
UB	Universitat de Barcelona
XPS	X-ray photoelectron spectroscopy
XRD	X-ray diffraction
XRR	Small angle X-ray reflectivity
XTEM	Cross sectional transmission electron microscopy
YBCO	Yttrium barium copper oxide ($YBa_2Cu_3O_{7-x}$)
YSZ	Yttria-stabilized zirconia
YSZ(IBAD)/SS	YSZ(IBAD)/Stainless Steel

APPENDIX 1

SUBSTRATE AND BUFFER LAYER STRUCTURES

SUBSTANCE	TYPE OF STRUCTURE	LATTICE PRAMETERS (Å)	MELTING TEMPERATURE (ºC)
$YBa_2Cu_3O_7$	Triple Perovskita	a=3.823 b=3.887 c=11.680	1100
CeO_2	Fluorita	a=5.411	2400
$BaZrO_3$	Perovskita	a=4.193	2600
$SrTiO_3$	Perovskita	a=3.905	2300
YSZ	Fluorita	a=5,139	2724
MgO	Rock Salt	a=4.217	2830
Ni	Fcc	a= 3.523	1453
NiO	Rock Salt	a=4.194	1960

Chapter 1

INTRODUCTION

1.1 SUPERCONDUCTING MATERIALS

One of the most notable events in this century has been the discovery of superconducting materials by Heike Kamerlingh Onnes of the Leiden University [1] in 1911. He observed that the mercury immersed in liquid helium had lost totally his electric resistance (fig.1.1).

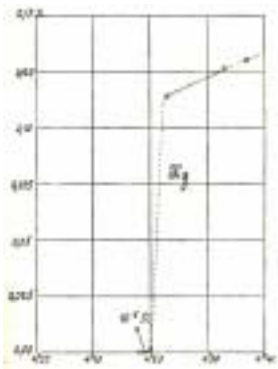

Fig. 1.1: Resistance in ohms of a specimen of mercury versus absolute temperature. This plot by K.Onnes marked the discovered of superconductivity.

The "superconducting dream" started in the early 1986 when two German physicists K.A. Müller and J.G. Bednorz [2] of IBM research laboratories discovered that a new compound, a member of the perovskite family with composition (La-Ba-Cu-O), became superconductor at 30K while at that moment the highest critical temperature, Tc, had been 23.2K for Nb_3Ge. The discovery of the cuprate superconducting materials excited all the scientific world. The idea of a superconductor at room temperature induced a real competition between different laboratories to find the superconductor with the highest T_c . The king of the cuprate family was found in the

early 1993, a mercury-based compound [3] with a transition temperature up to 164K under a pressure of 10^5 Pa.

1.1.1 AN HISTORICAL OVERVIEW

- ***1908*** H.K. Onnes succeeds in liquefying helium
- ***1911*** H.K. Onnes finds that the electrical resistance of Hg plumbed to zero at 4.2 K
- ***1913*** H.K. Onnes receive the Nobel Prize for Physics
- ***1933*** W.Meissner and R. Ochsenfeld [4] find that applying a magnetic field on a superconductor which is under its T_c, it repulses the magnetic flow from its interior as a diamagnetic material.
- ***1947*** Nb has the highest Tc (9.3 K) of the elements of the periodic table.
- ***1950*** L.D. Landau and V.L. Ginzburg, two Russian researchers, develop the first superconducting Theory [5] based on the free energy of a superconducting system.
- ***1957*** L.N.Cooper , J. Bardeen and T.R. Schrieffer postulate the "BCS Theory" [6] which can explain the superconducting properties of the low T_c superconductors.
- ***1964*** The first superconducting oxides, TiO and NbO with a T_c of 1 K are discovered.
- ***1972*** L.N.Cooper , J. Bardeen and T.R. Schrieffer receive the Nobel Prize for Physics.
- ***1975*** The first polymeric superconductor, $(SN)_x$, with a T_c<1 K is reported [7].
- ***1986*** K.A. Müller and J.G. Bednorz discover the first superconductor of high T_c, the cuprate $La_{1.85}Ba_{0.15}CuO_4$ with a T_c of 35 K [2] , first synthesized by C. Michel, L. Er-Rahko and B. Raveau.

- ***1987*** K.A. Müller and J.G. Bednorz receive the Nobel Prize for Physics.
- ***1987*** C.W. Paul Chu and M.K.Wu and co workers [8] synthesized a new cuprate, $YBa_2Cu_3O_{7-x}$ (YBCO) with a T_c of 93K, the first superconductor under liquid nitrogen.
- ***1993*** Discover of the $HgBa_2Ca_2Cu_3O_{8+\delta}$ with T_c of 130 K.
- ***Very recently*** new classes of superconductor have been found, fullerides such as MC_{60} (M =K_3,Rb_3,Cs_2Rb), boron- and fluorine-containing compounds such as $LnSr_2Cu_{3-x}BO_7$ and $Sr_{2-x}A_xCuO_2F_{2-\delta}$ (A= Ca or Ba), the oxycarbonates, and magnesium diborate.

1.2 SUPERCONDUCTING PROPERTIES

Usually we associate superconductivity only with the loss of the electrical resistance below a critical temperature called T_c. Above T_c the material is in its normal state. The absence of electrical resistance, however, does not completely define the superconducting state. The second important characteristic is called the Meissner-Ochsenfeld [4] effect. When a material makes the transition from the normal to the superconducting state, it actively excludes magnetic fields from its interior; this is called the Meissner effect. This constraint to zero magnetic field inside a superconductor is distinct from the perfect diamagnetism which would arise from its zero electrical resistance. Zero resistance would imply that if you try to magnetize a superconductor, shielding current loops would be generated to exactly cancel the imposed field. But if the material already had a steady magnetic field through it when it was cooled through the superconducting transition, the magnetic field would be expected to remain, as for a "perfect" conductor.

Applying an external magnetic field to a superconductor at a $T<T_c$, and increasing it until a particular value called critical magnetic field (H_c), the superconductor will change to its normal state. H_c depends on the temperature. The current density that flows

in a superconductor at a certain temperature and a fixed external magnetic field is called critical current density, Jc (fig.1.2).

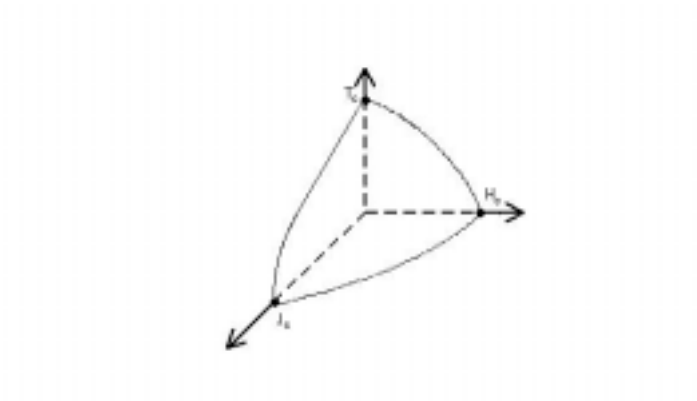

Fig.1.2: Characteristics of the superconductors: J_C, T_C and H_C.

1.2.1 PENETRATION DEPTH (λ) AND COHERENCE LENGTH (ξ)

In a superconductor there are two very important lengths, Penetration Depth (λ) and Coherence Length (ξ).

The shielding currents responsible of the superconducting diamagnetism are not totally confined in the material surface, but flow from the surface to the interior for a characteristic width. Consequently the magnetic flux will not decay drastically on the surface but exponentially at increasing distance from the surface. This distance length in which the decay takes place is called penetration depth (λ).

The Coherence length (ξ) is the measure of the spatial separation of Cooper electrons pair, see Cooper Theory [6]. At low T, these parameters λ and ξ have values practically constant and characteristic of the material (λo,ξo) , but increasing the temperature they quickly increase till become infinite for $T>T_C$.

1.2.2 TYPE I AND TYPE II SUPERCONDUCTORS

Type I superconductors behave as perfect diamagnetic materials, they will maintain the superconductor state until the external magnetic field outruns H_C. The type II superconductors behave as type I until a particular value of magnetic field called H_{c1} (lower critical magnetic field). When the field increases they do not pass in a normal state but in a so called "mixed state" or "Vortex state". The magnetic field starts to penetrate in the material constrained in filaments called vortex until reaching a magnetic field called H_{c2} (upper critical magnetic field). Above H_{c2} the superconductor goes back to its normal state (fig.1.3).

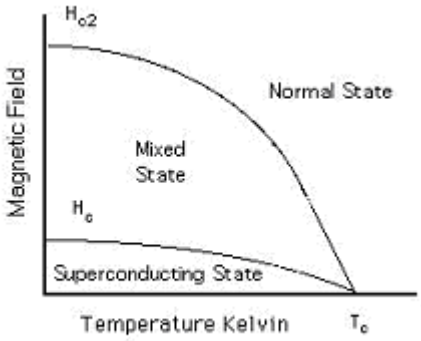

Fig.1.3: Type II Superconducting materials. In the mixed state the magnetic flux penetrates in form of vortices.

The characteristics of the coherence length and the penetration depth permit to define the two categories, type I and II. In type I superconductors ξ is greater than λ.

These materials generally are superconductors at low temperature and low magnetic field. If the field reaches the superconductor critical value, it penetrates the material destroying the superconducting state. In the type II the Penetration depth is greater than the coherence length and the superconductors remain in superconducting state also after the magnetic field penetration. The type II can stand higher magnetic fields than type I. Actually while H_{c1} for type II is similar to H_c of type I, H_{c2} has a higher value, by two order of magnitudes.

Since type II Superconductors can transport greater electric current without loosing their superconducting properties, they are more suitable for technological applications.

1.2.3 IRREVERSIBILITY CURVE

In type II superconductors there is the zone between H_{c1} and H_{c2}, where the external magnetic field can enter inside the material in form of vortices without destroying the superconductivity. The vortex which penetrates from the surface, moves inside the material until finding a position in which the total energy of the system is minimised. This energy depends on the particular temperature and magnetic field value under which the material is submitted. Usually the vortex finds micro-structural defects of the material where getting "pinned". If the magnetic field and the temperature are high enough but however under H_{c2} and $T_{c,}$ the vortex will move inside and out of the material without getting pinned. In this condition the superconducting J_c is zero. The irreversibility curve divides the mixed state in two zones, one where the vortex are "pinned" and J_c is different from zero and the other one where the vortex moves and J_c is zero. The irreversibility curve can change inside the mixed state due to the presence of different quantity of micro-structural defects of the material which can act as pinning centres. In fig.1.4 it is presented the irreversibility curve of some HTc superconductors.

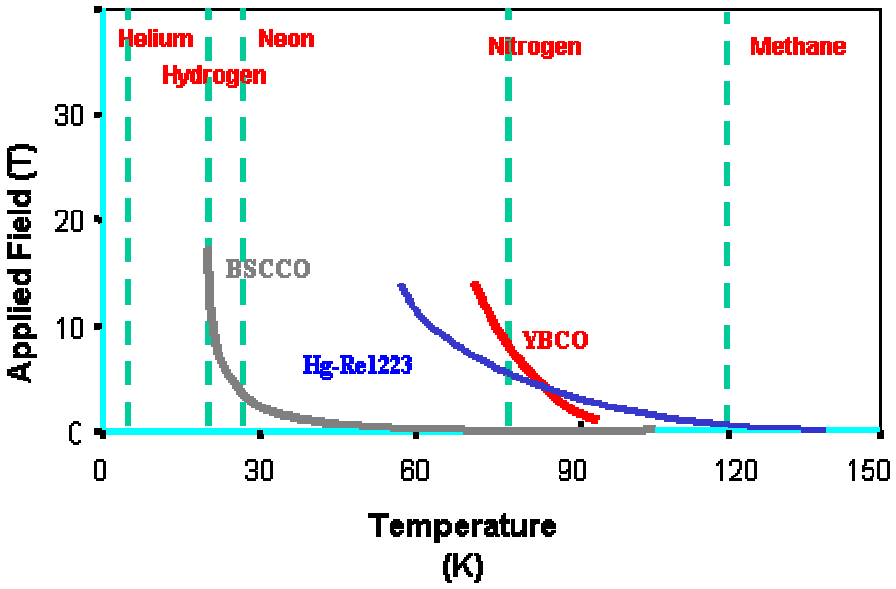

Fig.1.4: Irreversibility lines of higher T_C cuprate superconductors. At 77K, (liquid nitrogen), YBCO has the highest irreversibility magnetic field.

1.3 CONTEXT OF THE PRESENT RESEARCH

Large-scale superconducting electric devices for power industry depend critically on wires with high critical current density at temperatures where cryogenic losses are tolerable [9].

The feasibility of superconducting power cables, transformers, fault current limiters, motors and magnetic energy-storage devices, largely using $(Bi,Pb)_2Sr_2Ca_2Cu_3O_x$ conductor [10], has been demonstrated. Fermilab, Brookhaven, Desy and Cern laboratories all have accelerators composed of kilometres of superconducting bending and focusing magnets [11]. Only the medical application of superconducting materials is a commercial business now exceeding US $ 3 billion per year. Nevertheless in the early future superconductivity could have a significant role in deregulated electricity markets and in lessening CO_2 emissions.

Superconducting tapes must have sufficient strength to withstand the fabrication process, and sufficient size to carry operating currents from hundred to thousand of amperes at cost comparable to Cu wires. The estimations of the acceptable cost for industrial application are in the range of US $10 to US $100 per kAm.

As coordinator of the European project Solsulet, the unique in Europe that assumes the challenge of developing low cost coated conductors by CSD (Chemical Solution Deposition) in Europe, our group assumed the huge aim of engineering a pilot system that should produce a superconducting power cable of ten meters length.

For each different superconducting device, the target of current density J_c, operating temperature, and field is different; in Table 1.1 all these values are resumed [9]. To project a superconducting power cable, we have to consider these important target values: current densities must attain 10^5 A cm^{-2} at 77 K (liquid nitrogen temperature) in a magnetic field of less than 0.2 T.

TABLE 1.1: Industry consensus for wire performance requirements for various utility devices.

Application	J_c (A/cm^2)	Field (T)	Temperature (K)	I_c (A)	Cost (US$ per kA m)
Fault current limiter	10^4-10^5	0.1-3	20-77	10^3-10^4	10-100
Large motor	10^5	4-5	20-77	500	10
Generator	10^5	4-5	20-50	>1000	10
SMES*	10^5	5-10	20-77	~10^4	10
Transmission cable	10^4-10^5	<0.2	65-77	100 per strand	10-100
Transformer	10^5	0.1-0.5	65-77	10^2-10^3	<10

*SMES, superconducting magnetic-energy storage.

A High temperature operating value is important to reduce the cost of superconductor cable refrigeration.

Table1.2 [9] presents five type II superconductors and their critical current density relevant parameters, important to select the more proper candidate to become a superconductor power cable.

TABLE 1.2: Basic material and critical current density relevant parameters for practical superconductors.

Materials	T_c (K)	H_{c2}	H^*	Critical current density (A cm^{-2})	$P(T_c)$ (μΩ cm)
Nb4 7wt%Ti	9	12 T (4K)	10.5T (4K)	$4 \cdot 10^5$	60
Nb_3Sn	18	27 T (4K)	24T (4K)	~10^6	5
MgB_2	39	15 T (4K)	8T (4K)	~10^6	0.4
YBCO	92	>100 T (4K)	5-7T (77K)	~10^7	~40-60
Bi-2223	108	>100 T (4K)	~0.2T (77K)	~10^6	~150-800

The first choice is limited by operating temperature of 77 K (liquid nitrogen); of the five only $YBa_2Cu_3O_{7-x}$ (YBCO) and $Bi_2Sr_2Ca_2Cu_3O_x$ (Bi-2223) have a higher T_c.

Applications are limited also by a lower characteristic field, the irreversibility field $H^*(T)$ at which J_c vanishes. Bi-2223 has a low irreversible field at 77K (0.2-0.3T) which restricts its applications, while YBCO looks like more powerful with its $H^*(77K)$ ~7 T that means a supported higher current flux at 77K. There are many processes for producing YBCO superconductor and ceramic buffer layer thin films. Typical ones are

PLD (Pulsed Laser Deposition) [12-15], sputtering, metalorganic chemical vapour deposition [16-17], thermal evaporation [18,19], MOD (metal organic deposition) [20-22] and the sol gel process. All vacuum processes as PLD and Sputtering , permit to obtain high quality YBCO and buffer layers, however the high cost of vacuum technology and the low scale up facility , do not make them suitable for producing long electric power superconducting tapes.

In the last years the sol-gel coating technology has been developed as an alternative solution, just because it does not need any vacuum apparatus and could reduce the production cost while keeping similar material performances.

1.4 $YBa_2Cu_3O_7$ SUPERCONDUTING COATED CONDUCTOR

$YBa_2Cu_3O_{7-x}$ (YBCO) is a ceramic material with the perovskite structure (fig. 1.5). It has an orthorhombic unit cell, consisting of three perovskite units stacked along the c-axis.

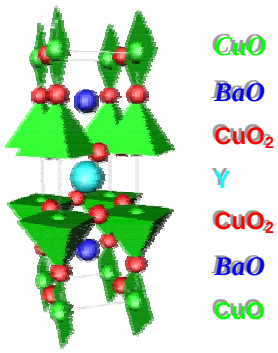

Fig. 1.5: Orthorombic unit cell of the YBCO.

YBCO is a complex, layered perovskite where the central unit contains the yttrium cation, around which are stacked the CuO_2 planes of strong superconductivity. The Cooper electron pair moves in CuO_2 planes perpendicular to the c-axis of the YBCO cell. All HTc cuprates have a high anisotropy. Experimental data indicate that electric conductivity is higher in a/b CuO_2 planes than in the perpendicular direction (c-axis).

The YBCO anisotropy is defined by the resistivity coefficient (γ):

$$\gamma^2 = \frac{\rho_c}{\rho_{ab}}$$

For YBCO γ^2 is ~50, notably smaller compared with the higher T_c cuprate Bi-2223 that has γ^2 ~20000. The difference is that while in the YBCO two CuO_2 planes are intercalated by normal metallic planes in the Bi-2223 the intercalate planes are insulating. The anisotropy imposes the need of a high degree of texture in order to align the superconducting CuO_2 planes. It is necessary a biaxial texture to avoid weak grain links which could block totally or partially the current flux between grains. All grain boundaries with more than 5° of misalignment will reduce the total current amount which could pass through the superconductor material by a factor of two or more as shown in fig. 1.6.

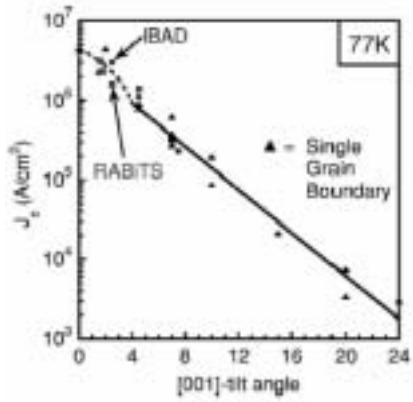

Fig. 1.6: Transport critical current density at 77 K measured in thin film bicrystals of YBCO as a function of misoriantation, θ. $J_C(\theta)$ exhibits an exponential dependence on θ.

A superconductor material with a high epitaxy level (fig.1.7(a,b)), do not present many weak grain unions and the electric current which could be transported will be maximum.

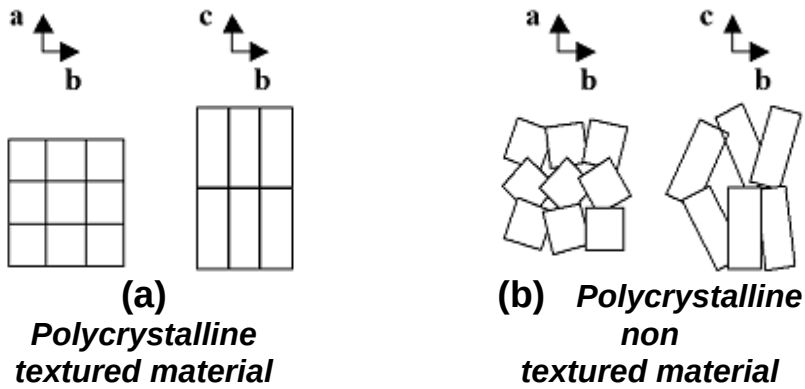

Fig. 1.7(a,b): Policrystalline materials: (a) well textured material with non weak unions while, (b) is a non-textured material.

To obtain such a biaxially oriented material, it is necessary a seed or substrate in order to induce this kind of growth, a material with the desired structure and orientation which could influence the YBCO growth. This process is called epitaxy and materials grow in this way as epitaxial layers.

Nowadays using the thin film technology, several meters of epitaxial YBCO film on biaxial metallic substrate have been obtained. The best result is a thin film with a J_c of 1 MA cm^{-2} at 77K of one meter long, one centimetre width, and one micron thick [23]. Thin film YBCO on metal substrates has also better tensile properties, due to the reduced thickness with respect to the bulk material, and to the metal properties of the substrate. There are several technical metal substrates which could be useful:

1) The Nickel RABiT (Rolling Assisted Biaxial Texturing) [24], a metal textured by a cold lamination.
2) The SOE (Self Oxidation Epitaxy) [25,26] Nickel Oxide with a biaxial texture. A layer of Nickel(RABiT) is oxidised by a thermal controlled process.
3) The YSZ (Yttrium stabilised Zirconium oxide) deposited by IBAD (Ion Beam Assisted Deposition) [27] on a Stainless Steel substrate. A film of ceramic material in this case YSZ is deposited on a polycrystalline substrate and biaxially textured by an Ion Beam.

Almost all metal substrates react with YBCO and oxygen at high temperature, that is why it is important to protect the substrates by growing an inert film called "Buffer Layer" in-between YBCO and the metal substrate.

It appears obvious that the quality of the buffer layers is critical since it must transmit the texture to the YBCO film and acts as a diffusion barrier in order to avoid contamination of the film as well as oxidation of the substrate.

The future architecture of the superconductor power cables will be something like that shown in fig 1.8(a,b).

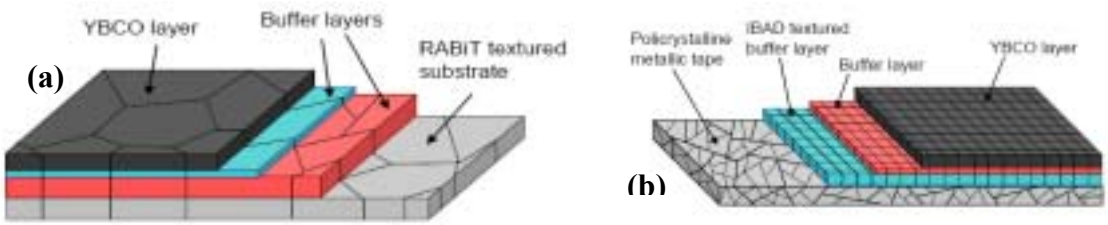

Fig. 1.8(a,b): Structure of two different textured coated conductor. Typically the metal substrate is protected by several buffer layers. Template architectures for (a) NiO(SOE)/Ni(RABiT) and (b) YSZ(IBAD)/SS substrates.

1.5 SOL-GEL ROUTE

The Sol-Gel chemistry first discovered in the late 1800s had a renewed interest [28] in the early 1970s when monolithic inorganic gels were formed at low temperatures and converted to glasses avoiding a high temperature melting process. Nowadays applications of sol-gel processing include such different areas as ceramic processing, novel glasses, fibres, abrasives, antireflection coatings, absorbing coatings, filters for light and optical purposes, semiconducting coatings and protective layers, to name only a few.

The sol-gel method is a technique for forming glass and ceramic materials from liquid metalorganic precursors by polymerisation reactions. In essence, the process begins by hydrolysis and polycondensation of precursors in solution, using a suitable catalyst, to form a colloidal suspension of nanometer scale particles (sol). This sol is then coated onto a surface or cast into a mould, after which further condensation produce a rigid network (gel) [29] (fig.1.9).

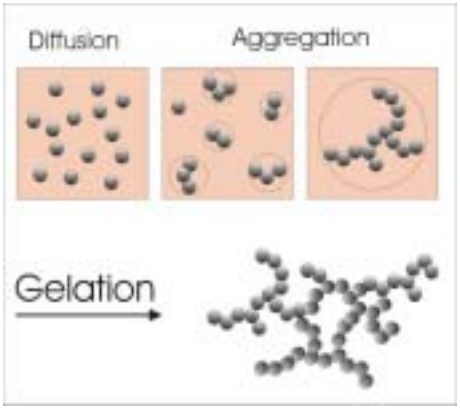

Fig. 1.9: Gels are formed by chemical or physical reactions of small sub-units (molecules, polymers or colloids).

The precursors for synthesizing these colloids consist of a metal or metalloid element surrounded by various organic ligands.

We can summarize the sol-gel route in three main parts: the precursor solution preparation, the deposition process, and the thermal crystallization. Each part of the process is fundamental to control the properties of the materials that we want to synthesize.

1.5.1 OVERVIEW OF THE CHEMICAL SOLUTION DEPOSITION (CSD) PROCESSES

First of all it is better clarify the nomenclature of the sol-gel processes. Usually all the chemical processes are generically referred to sol-gel. R.W.Schwartz in its review [30] renames all the chemical methods (mainly three), used in thin film technology as Chemical Solution Deposition (CSD):

1. The **sol-gel metal-organic** route using metal alkoxides as precursors in organic solvents[31-33]. Normally the metal ligand is a deprotonated alcohol. For example, in perovskite synthesis the 2-methoxyethanol is the typical route.
2. The **Chelate processes** are a modification of the metal-organic route, some chelant substances are added to the solution, for example some organic acid or deprotonated ones, as acetic acid or acac (acetylacetonate) [34-36].
3. The Metal Organic Decomposition (**MOD**) uses water insensitive precursors as metal-carboxylate compounds [37-39].

Another sol-gel process rarely used in thin film preparation is the **Inorganic route** with metal salts in aqueous solution (chloride, oxychloride, nitrate [40] etc.): much cheaper and easier to handle than metal alkoxides, but usually with wettability problems during deposition by spin or dip coating.

Let's see in detail each one of the three CSD processes:

The **sol-gel route** : the precursors materials, metal-alkoxide reactives $M(OR)_x$ are dissolved in organic solvents. At the functional group level, three reactions are generally used to describe the sol-gel process: hydrolysis, alcohol condensation, and water condensation (fig. 1.10(a,b,c)).

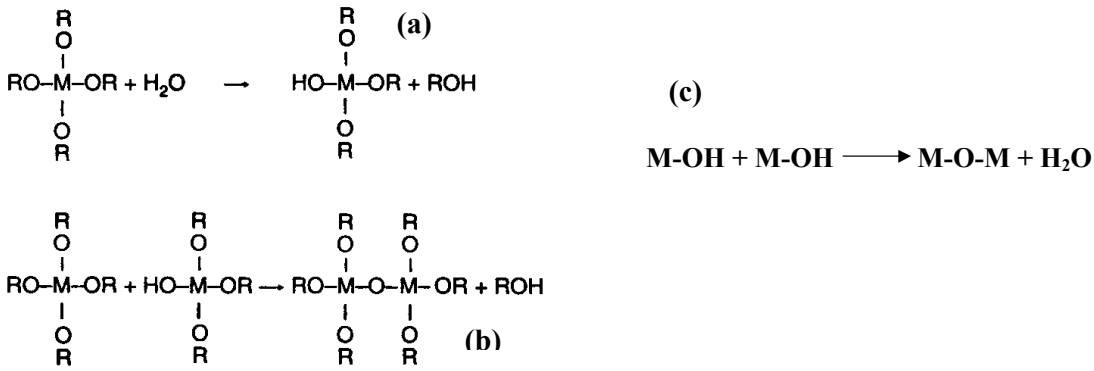

Fig. 1.10(a,b,c): Typical reactions of hydrolysis (a), alcohol condensation (b) and (c) water condensation.

In this way, oligomeric species with M-O-M bonds form in the precursor solution. Controlling the H_2O/Metal ratio, type of catalyst , pH solution, complexing ligands, dopants, solvent nature ,and the process temperature , it is possible to control the gel clusters shape and size and consequently the properties and porosity of the future ceramic material.

The main problem of this process is the use of metal-alkoxides precursors, which are usually very sensitive to the atmosphere humidity.

One of the most useful organic solvents employed is the methoxyethanol ($CH_3OCH_2CH_2OH$). Its use has two main reasons: as solvent it could dissolve quite every kind of metal-alkoxyde, and usually it is less reactive with water than other alkoxides, simplifying the solution manipulation. The alcohol exchange reaction could explain this methoxyethanol behaviour:

$$M(OR)_n + x(CH_3OCH_2CH_2OH) \longrightarrow M(OR)_{(n-x)}(OCH_2CH_2OCH_3)_x + M(OR)_x$$

The substituted metal-alkoxy compound is now well dissolved in methoxyethanol and it is less sensitive to humidity. Usually this reaction needs a reflux process and is controlled by a distillation.

The key points of the **sol-gel processes** could be summarized as follow:

- Formation of oligomeric species which can be controlled in size and shape.
- High control and reproducibility of the process
- Minimal aging effect of the solution
- Complex chemistry: needs to work in an inert atmosphere, and perfect control of distillation and reflux processes.
- Teratogenity of the 2-methoxyethanol normally used in this kind of process.

The **chelate processes:** as for the sol-gel, the reactives are metal-alkoxide, but to control better the hydrolysis, chelate agents have been added, as β-diketone, acetic acid or some kind of ammine compounds. Chelation plays an important role, for example:

$$M(OR)_n + xCH_3COOH \longrightarrow M(OR)_{n-x}(OOCCH_3)_x + xROH$$

At this point, hydrolysis and condensation lead to small oligomers formations [41-42]. Normally a volume of water or methanol is added to control the solution viscosity and stability. In presence of an acid, as acetic acid, and alcohol reactions of esterification are also possible.

In the solution, after weeks to months, due to the presence of unreacted alkoxide groups, reactions of hydrolysis condensation or esterification can take place.

For the **chelate processes** we would like to emphasize the following points:

- Simpler solution preparation, without the distillation and refluxing processes as described by Schwartz et al. and Yi and co-workers [34,35].
- Formation of smaller oligomers
- Reduction of the water sensitivity of the chelated metal-alkoxides.

- Diminution of the ability to control the precursor solution structure compared to true sol-gel approaches.
- Solution aging.

The **MOD processes:** in the Metal-Organic Decomposition hydrolysis and condensation have a marginal effect with little or no clusters formation. Basically the solution is prepared by dissolving reactives with large carboxilate chains in common solvents. As the large organic chains may cause film cracking or shrinkage during the weight loss in the thermal treatment, recently Heartling [38] has developed an alternative strategy to avoid these problems. In the new process short carboxylate-chain, as acetic acid, or β-diketonate (acac) have been used.

In the MOD processes there is no proper suspension, but more or less a solution which polymerises only when overcomes the critical concentration value. The polymer is kept together by Van Der Waals or Hydrogen bonds. This kind of polymerisation is easily reversible to the solution state by only adding new amounts of solvent to the polymer. MOD-Sol-Gel has limited mechanical properties but enough to resist over a substrate till the thermal treatment eliminates the film organic part. It is a soft chemical method, simple to scale up and economically attractive. In chapter 3, the MOD- route to prepare cerium oxide buffer layers, and in chapter 7, the MOD-TFA systems are presented.

The key points of the **MOD processes** could be summarized as follows:

- Fast and "easy chemistry" to prepare the precursor solutions.
- Water insensitive and absence of oligomerization.
- Solution aging slower than in the chelating processes [30].
- Cracking due to the loss of weight in the crystallization process using large carboxylate reactives.
- Impossibility to "tailor" the properties of the materials, due to the absence of reaction of hydrolysis, condensation or esterification which well controlled permit to pilot the micro-structural characteristics of the thin-films.

Advantages of the CSD Techniques:

- High purity.
- No need of vacuum technology.
- High degree of homogeneity, because reagents are mixed at molecular level.
- Porosity control, low or high, by using the appropriate CSD system and heat treatment.
- Possibility to obtain fully-dense crystalline ceramics which cannot be prepared by conventional powder processing.
- The capability of obtaining fully-dense amorphous solids at temperatures lower by hundreds of degrees than those required for conventional compaction/densification or for melting.

Drawbacks :

- Long processing time.
- Many synthesis parameters to control.

1.5.2 DEPOSITION PROCESSING

One of the advantages of the CSD techniques is without doubt the deposition step. It is easy to deposit over a large surface or to insert a deposition apparatus in an industrial continuum process thus reducing costs.

The principle of the CSD deposition techniques is that a homogeneous film forms due to the evaporation of the excess solvent (gelification). Gelification could be obtained principally in two ways depending on the kind of CSD precursor solution used.

In sol-gel usually gelification is the result of the condensation reaction between clusters during the solvent evaporation. In chelate and especially in MOD processes during the solvent evaporation the small clusters (Chelate) or the molecule (MOD) arrive to a such concentration that gelification happens via Van der Valls and Hydrogen bonds formation (physical polymer).

One of the parameters that is possible to control during this step is the thickness of the film, at the same conditions (concentration and viscosity) of the precursor solution, the parameters of deposition could influence the final thickness of the film.

The sol-gel deposition systems are simple and basically three:

1) **Dip-coating**, where the part of the substrate to be coated is withdrawn from a solution. This system is usually used in industrial manufacturing to obtain a continuum process, as the pilot one in fig. 1.11 projected to deposit YBCO in a future industrial application.

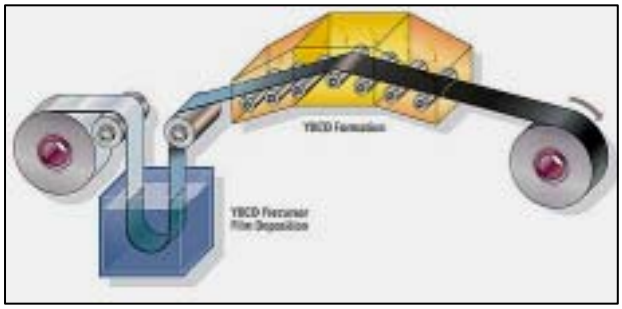

Fig. 1.11: Scale up of a dip coating system

This method is also used at laboratory scale. Controlling the withdrawal rate of the substrate it is possible to modify the thickness of the film.

The higher is the withdrawal rate, the thicker will be the film.

2) **Spin-coating** , where the liquid film is spread out by spinning. Fig. 1.12 shows the three main parts of this method, dispense, ramp-up and constant rotation.

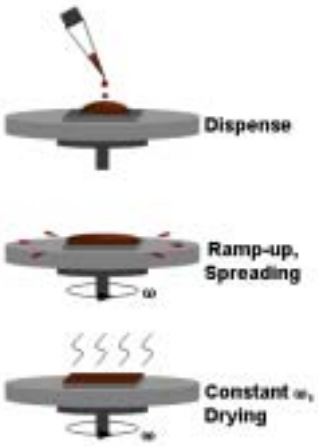

Fig. 1.12: Spin coating procedure. Once dropped the solution on the substrate fixed to the spinner, the acceleration and speed rotation make the solvent evaporate and the film gellify.

This method is typically used at lab-scale: a certain volume of solution is deposited by a syringe on a substrate fixed at a rotating plate. The plate rotates with a certain rate, acceleration, and for a fixed time. In this way the solvent in excess evaporates and the film gellified. The solution volume depends on the substrate size, and it has to be enough for a complete coverage, this is important to avoid defects in the film.

Commercially some spinners can also control the inner atmosphere, by introducing gasses, or heat the rotating plate favouring the gel formation.

Many different parameters have to be controlled to obtain a really homogeneous film as reported by D. P. Birnie group [43].

3) **Spry-coating** where the surface is sprayed with fine disperse solutions. This is a really industrial system. The substrate rate and solution characteristics (viscosity and concentration) are strictly correlated with the deposited film thickness. In fig. 1.13 is represented a scheme of a possible spry system.

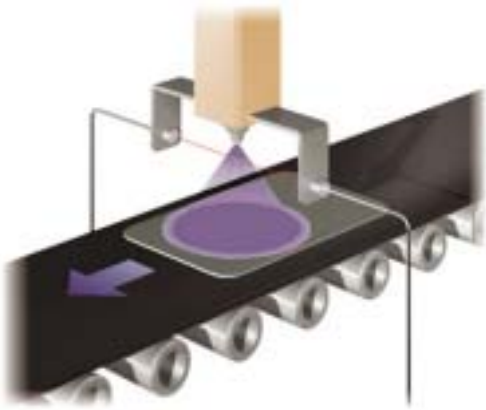

Fig. 1.13: Spry coating apparatus.

There are different studies on how to spray the precursor solution in fine dispersed particles. One very promising seems to be an ultrasound one that is able to produce a very homogeneous dispersion of the precursor solution. The spry coating is not useful for all kind of precursor solutions because the interactions between micro drops after deposition have to be strong enough to obtain a homogeneous film on the substrate.

1.5.3 THERMAL CRYSTALLIZATION

Typically, after deposition the film has a thickness that, depending on the CSD process used, could be 10 times thicker than after crystallization. During the thermal treatment, the loss of the organic part of the gel network, (Pyrolysis), may cause undesired phenomena which worsen the film properties. The film shrinkage, for example, occurs because of the capillary forces due to the rapid volume changes in the film. Thus it is important to control the phenomena which occur during the gel conversion into a crystalline ceramic material.

Before the crystallization (nucleation and growth), the film undergoes chemical and physical transformations. The pyrolysis is typically performed between 200ºC-400ºC, the organic part and the solvent that is retained in the gel network are burnt out.

In this step the M-O-C (or M-O-H) bonds start to be broken in favour the formation of M-O-M bonds. After pyrolysis the material is still a quasi amorphous

inorganic film with eventually some organic inclusions that still persist. At a little higher temperature of the pyrolysis, the material that now is quite porous, starts a structural rearrangement, called densification. Depending on the reactive and on the thermal ramp, densification can occur either before or after the crystallization. Usually the thin film technology, especially for textured materials, prefers a dense microstructure. The densification of a material prior to crystallization is led by structural relaxation and viscous flow, instead of solid-state sintering (densification after crystallization). Since solid-state sintering is energetically less favourable and it is a long process, densification before crystallization is preferred and normally leads to denser materials.

There are two different approaches to the thermal crystallization, one step or two steps processes. In the one step process the film is heated rapidly, in this way it is possible to delay the onset of crystallization to a higher temperature, reaching a higher material density. In the two step process instead, the pyrolysis is separated from the crystallization with a thermal dwell at pyrolysis temperature.

It is possible to summarize the crystallization process in the following points:

- Condensation reactions
- Pyrolysis
- Densification
- Nucleation
- Crystal growth

1.5.4 CRYSTAL GROWTH (THERMODYNAMIC AND KINETIC MODELS)

Nucleation and growth are associated to a favourable thermodynamic contribution, ΔG_V, the free energy per volume of material created, and an unfavourable one, the surface energy, ΔG_S due to the formation of new surface. Surface energy exists because bonds are broken to create (or increase) a surface.

$$\Delta G=\Delta G_V+\Delta G_S$$

The minimization of the surface energy could be a strong driving force that influences the nucleation and growth of a material. The ΔG_S term can be represented as shown in fig. 1.14.

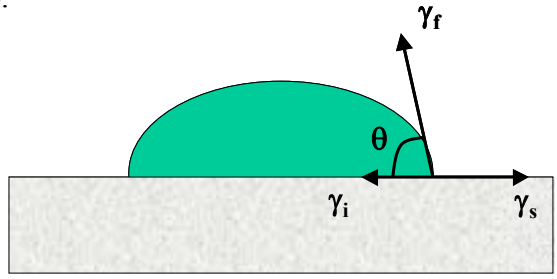

Fig. 1.14: Energy contributions during the film nucleation.

γ_i : interface energy (substrate/interface), the free energy per unit of interface area.

γ_s : surface energy of the substrate, the free energy per unit of the substrate free area.

γ_f : surface energy of the film, the free energy per unit of film free area.

$$\Delta G_S = \Sigma \gamma_j \cdot A_j$$

The relative magnitudes of these energies strongly influence nucleation and growth.

$\Delta G_S =$	$\alpha_1 r^2 \gamma_f$	curved surface of nuclei
	$\alpha_2 r^2 \gamma_I$	interface
	$-\alpha_2 r^2 \gamma_s$	substrate surface

As Teichert [44] resumed depending on the contribution of each term, the crystal growth could be mainly of three types, fig. 1.15:

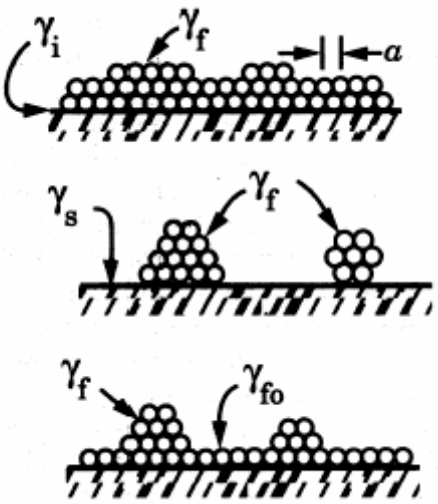

$\gamma_i + \gamma_f < \gamma_s$ Layer-by- layer growth (Frank-van der Merwe)

$\gamma_i \sim \gamma_f + \gamma_s$ Islands growth (Volmer-Weber). Minimization of total surface energy. Low γ facets islands formation.

$\gamma_i > \gamma_f + \gamma_s$

ML layer by layer that evolved to island growth (not only γ - effect) (Stranski-krstanov)

Fig. 1.15: Classial types of thin film growth.

In the vacuum systems generally the substrate is already at the temperature of nucleation and growth when the material starts to be deposited almost atom by atom. On the contrary in CSD, the material is deposited at room temperature and heated gradually to a maximum T where it transforms from an amorphous state to a crystalline one. Thus in the vacuum processes the material always nucleates on the substrate and the way it grows is strongly controlled by the minimization of surface energy. In CSD instead, it is not obvious that the film will nucleate on the substrate and its growth depends also on other factors besides the minimization of the surface energy as we will see in the following paragraph.

To study nucleation and growth of the CSD processes we apply the theoretical approaches employed for glass crystallization [45].

The nucleation step can be:

Homogeneous: in the particular case of a thin film grown on a substrate, it means that the nucleation happens throughout the total film thickness.

Heterogeneous: nucleation is energetically favoured on the surface on which the amorphous film is deposited.

From the thermodynamic point of view the energetic contribution to homogeneous nucleation is the free energy difference associated with the solid state transition (crystal formation), W^*. The volume creation during nucleation is energetically favourable and acts as a driving force. The new surface creation instead, acts as an energetic barrier as for vacuum processes, see fig. 1.16.

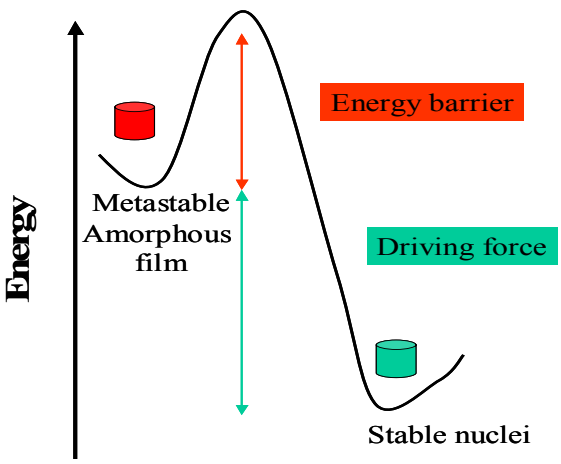

Fig. 1.16: Free energy control of the amorphous film nucleation.

Fig. 1.17 shows the difference in free energy between the solution-derived amorphous film and the crystalline phase, Roy [46]. It is clear that below the melting temperature nucleation is thermodynamically favourable and occurs throughout the film. Above the material melting point instead, the liquid phase is thermodynamically favoured.

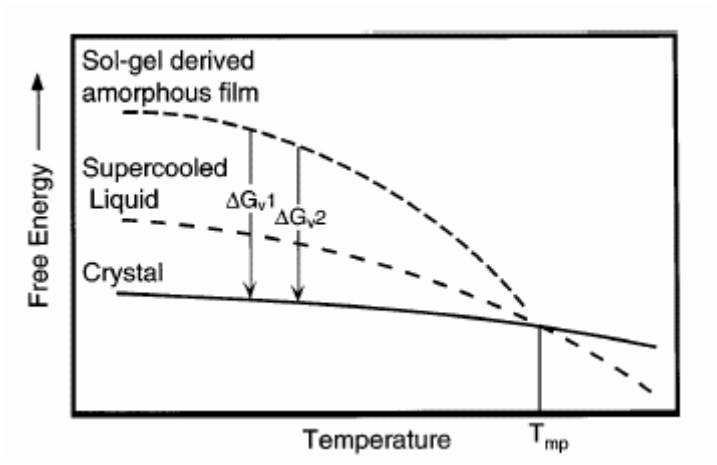

Fig. 1.17: Schematic representation of free energy-temperature relation among amorphous film and crystal at the same composition. It may be noticed that usually the amorphous film has a higher free energy than the glass at a temperature below of the melting point of the given composition [44].

The thermodynamic driving force to transform a volume of amorphous material in a crystal is the free energy difference ΔG_V (per volume). If "r " is the spherical radius of the nucleus the free energy difference will be: $\Delta G_V \cdot$volume of the sphere ($[4/3]\ \pi r^3$).

The creation of new surface opposes to nucleation and acts as a barrier, its thermodynamic contribution can be expressed by: surface energy or surface tension (γ)·surface area ($4\ \pi r^2$). Remember that on a substrate the surface tension γ is described by three components (γ_i , γ_f, γ_s)as seen at pag.22 (vacuum processes). Therefore, we can write:

$$W = \frac{4}{3}\pi \cdot r^3 \cdot \Delta G_V + 4\pi \cdot r^2 \gamma \qquad \text{(Eq.1)}$$

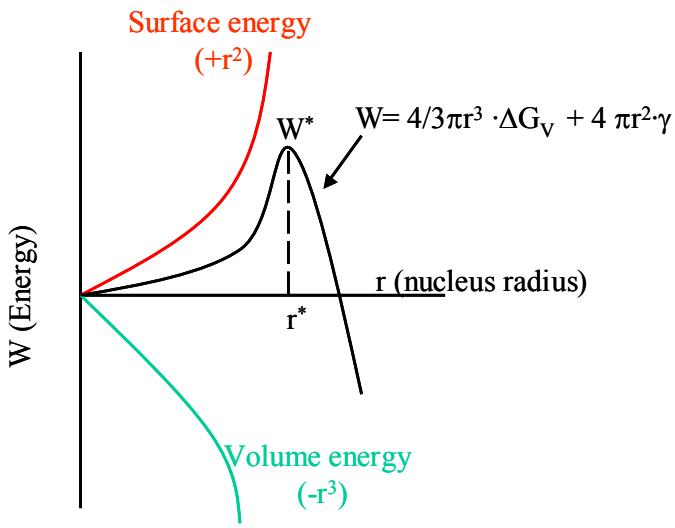

Fig. 1.18: The free energy of crystalline nucleation is correlated with two opposite energies; the positive surface energy and the negative volume one.

For small nuclei ($r < r^*$) the surface term dominates and the nuclei tend to re-dissolve; an increase in r causes an increase in W. On the contrary if the nuclei reach its critical size, energetically the volume term prevails, W decreases and that nuclei grow.

The maximum value of r^* it is the maximum of the W function in fig. 1.18:

$$\frac{dW}{dr} = 0 = 4\pi \cdot r^2 \Delta G_V + 8\pi \cdot r\gamma$$

This equation is solved for

$$r = r^* = \frac{-2\gamma}{\Delta G_V}$$

Replacing the r^* value in the W, equation 1, the thermodynamic barrier results:

$$W^* = \frac{16}{3}\pi \cdot \frac{\gamma^3}{\Delta G_V{}^2} \qquad \text{(Eq.2)}$$

It is clear that the thermodynamic barrier depends directly on the γ value, and when γ is reduced the nucleation is promoted.

In a large range below the melting temperature, the ΔG_V term predominates on the surface term ΔG_S and if the diffusion kinetics is favourable nucleation takes place throughout the total thickness of the film. In order to grow textured materials, single crystal substrate must transfer directly its crystallographic structure to the film; it means that it is preferable to force heterogeneous nucleation on the substrate.

The substrate-film interaction reduces the surface energy, leading to a reduction of the energetic barrier W^*, thus favouring the heterogeneous nucleation as shown in fig. 1.19.

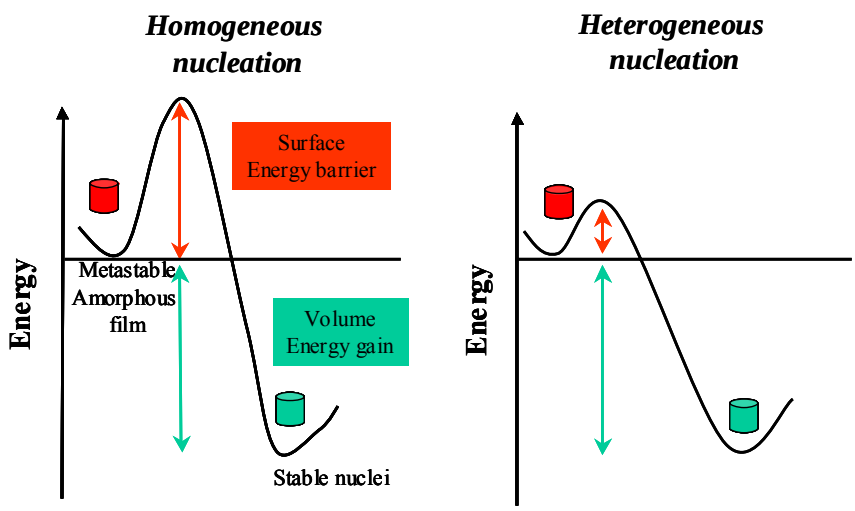

Fig. 1.19: The substrate-film interactions reduce the surface energy barrier and make easier the heterogeneous nucleation on the substrate.

When a liquid phase wets a substrate, (fig. 1.20), its surface tension is directly determined by the wetting angle (θ), the smaller is θ the smaller is the surface tension and more favourable will be the heterogeneous nucleation.

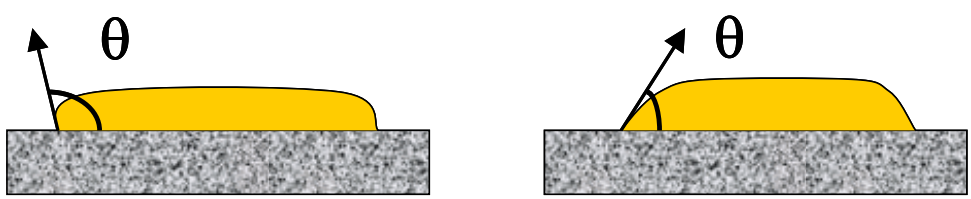

Fig. 1.20: Wetting angle is correlated with the film surface tensions.

We expressed the energetic barrier to homogeneous nucleation as:

$$W_{HOM}* = \frac{16}{3}\cdot\pi\cdot\frac{\gamma^3}{\Delta G_V{}^2} \qquad \text{(Eq.3)}$$

The relation between the surface tensions is (fig. 1.14):

$\gamma_S = \gamma_i + \gamma_f \cdot \cos\theta$

We can therefore express the energetic barrier for heterogeneous nucleation as a function of the homogeneous one:

$$W_{HET}* = W_{HOM}*\cdot f(\theta)$$

Where $f(\theta) = \frac{(2+\cos\theta)\cdot(1-\cos\theta)^2}{4}$

$$W_{HET}* = W_{HOM}*\cdot\frac{(2+\cos\theta)\cdot(1-\cos\theta)^2}{4}$$

$$Lim_{\theta\to 0} f(\theta) = 0$$

$$W_{HET}* = 0$$

When the wetting angle is near zero, the energetic barrier to heterogeneous nucleation is also near zero. Nevertheless as we will see later this is not a sufficient condition for heterogeneous nucleation to occur. If ΔG_V is too large compared with the barrier, as shown in Eq.3, homogeneous nucleation can still predominate.

To estimate the range of the domains of the two types of nucleation it is better to express the thermodynamic driving energy as:

$$\Delta G_V \approx \Delta H_V \cdot \frac{T_m - T}{V_m \cdot T_m} \qquad \text{(Eq.4)}$$

ΔH_V is the heat of fusion, V_m the molar volume and T_m the melting temperature. In order to induce heterogeneous nucleation, ΔG_V must be high enough to overcome W_{HET}^*, and small enough compared with W_{HOM}^*, to prevent homogeneous nucleation.

Inspection of eq. 4 easily reveals that ΔG_V can be properly tuned by adjusting the nucleation temperature. The smaller is the undercooling value, the higher will be the possibility for heterogeneous nucleation to occur.

On the other hand the lower is the temperature from the melting value, the greatest will be the driving force for homogeneous nucleation.

The Kinetic contribution ΔG_D, is the energy associated with the movement of material during the creation and growth of the nuclei. Nucleation is an activated process and could be described by Arrhenius equation:

$$I = A\exp\left\{\frac{-\left(W^* + \Delta G_D\right)}{k\,T}\right\} \qquad \text{(Eq.5)}$$

Where:

I is the homogenous nucleation rate

A is the pre-exponential factor

k is the Bolzmann's constant

W^* is the difference in free energy between the amorphous state and the nucleate one

ΔG_D is the diffusion energy in nucleation and growth

ΔG_D is related to how fast materials move to the surface of a growing nucleus, expressed as a diffusion coefficient.

$$D = \left(\frac{kT\lambda}{h}\right)\exp\left\{\frac{-G_D}{k\,T}\right\} \qquad \text{(Eq.6)}$$

Where λ is the atomic jump distance and D is is related to viscosity by the Stokes-Einstein equation:

$$D = \left(\frac{kT}{3\pi\lambda\eta}\right)$$

Hence the nucleation rate, I can be described by,

$$I = \left(\frac{Ah}{3\pi\lambda\eta}\right)\exp\left\{\frac{-W^*}{k\,T}\right\} \qquad \text{(Eq.7)}$$

It is interesting to note that the nucleation rate, I is inversely proportional to the viscosity $\mathbf{I \sim \eta^{-1}}$. High η it means low diffusion coefficient.

Much below Tm, ΔG_V increases, but nevertheless it is counterbalanced by the decrease of the nucleation rate due to the effect of η, as shown in fig.1.21.

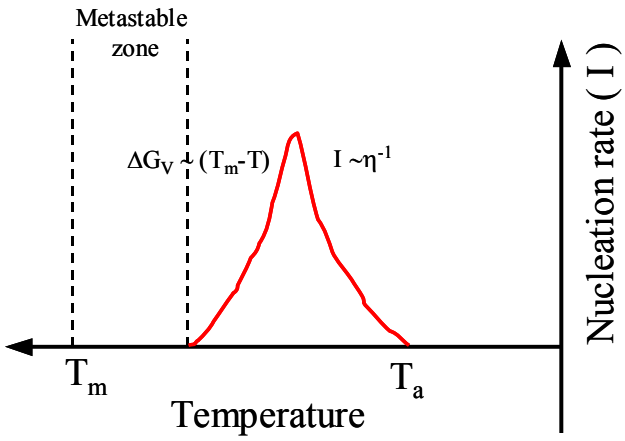

Fig. 1.21: The nucleation rate dependence with temperature. Its maximum value is function of the nucleation and growth diffusion energy and of the film viscosity.

Just below T_m there is a metastable zone in which the thermodynamic driving force is not enough high to overcome the energetic barrier due to the surface tension.

The grains that form are not able to reach the critical size r^* and nucleation is not favoured. Under the meta-stable zone there is a temperature at which nucleation rate is maximum.

1.5.5 HIGHLY TEXTURED FILMS BY CSD

The need to get highly textured CSD films sets us in front of a great dilemma, how to obtain heterogeneous nucleation on textured substrates if, as seen above, nucleation is normally favoured throughout the totality of the film thickness?

In the last years many laboratories have worked on CDS methods to produce a large number of different textured thin films. Some of them have developed processes to overcome this problem getting heterogeneous nucleation and so an epitaxial growth on single crystal substrates. One possibility is the choice of the substrate, if it has a good crystallographic match (as small as possible) with the material that we want to grow, the surface tension decreases (θ is small) and the heterogeneous nucleation is more probable. The other possibility is playing with the nucleation temperature as explained in the previous paragraph. Looking at the free energy graph, (fig.1.17), it is important to find a way to reduce the under cooling value (T_m-T_{nuc}), increasing the temperature at which nucleation starts. The bibliography reports basically two ways to obtain the heterogeneous nucleation; the first is using a fast heating rates in the synthesis, delaying in this way the nucleation step to higher temperatures next to the melting of the material, the other is using CSD precursors which have high decomposition temperature achieving the same effect of delaying the nucleation temperature.

In conclusion, it is important to underline that the CSD method has shown many advantages with respect to the vacuum systems, especially in the easy scale-up from laboratory to an industrial system or in the less expensive technology, but on the contrary in the production of high epitaxial thin films has presented a clear additional difficulty. For the CSD technology it is impossible to deposit a material layer by layer, and this is the main reason why usually, it is very difficult to reach the same high quality in the microstructure of the materials synthesized.

1.6 EXPERIMENTAL TECHNIQUES

1.6.1 X-RAY DIFFRACTION

The XRD diffraction measurements were performed on a Rigaku Rotaflex RU-200BV Diffractometer, in the Icmab-Csic, and the texture ones in a four-circle Goniometer Philips PW 3710 mpd control at the " Serveis cientifico Tècnics" of Barcelona University.

The condition for diffraction is that fulfils the Bragg law:

$$2d_{hkl}\text{sen}\theta = n\lambda$$

Where $\mathbf{d_{hkl}}$ is the distance between crystalline planes, **n** is the period, λ is the wave length of diffracted radiation (usually the copper one λ=1.5406 A°) and θ is the X-ray incident angle with the material surface. The X-rays could penetrate in the material till dozens of micros. In fig. 1.22 the four angles characteristics of Philips Goniometer have been represented, ω, θ, ϕ and ψ.

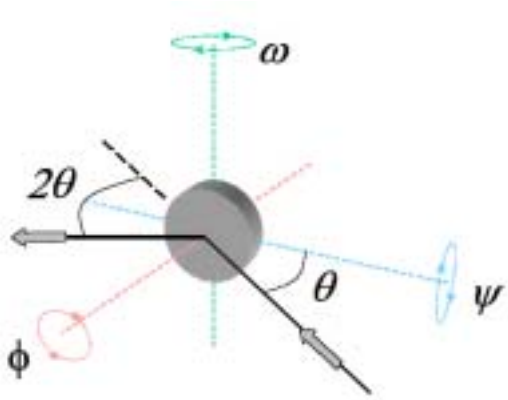

Fig. 1.22: Characteristic four angles of the Philips Goniometer.

θ/2θ-scan: We use the XRD **(θ/2θ)-scan** in the **2θ** range of 20-80 degree to observe the plane reflections of our samples and verify whether the film growth is epitaxial with the underlying substrate.

ω–scan: The *ω*–angle between the X-ray source and the sample is fixed and the detector moves In this way it is possible to observe the texture out-plane of the sample grown , in other words to see the reciprocal position between grain and grain (fig. 1.23).

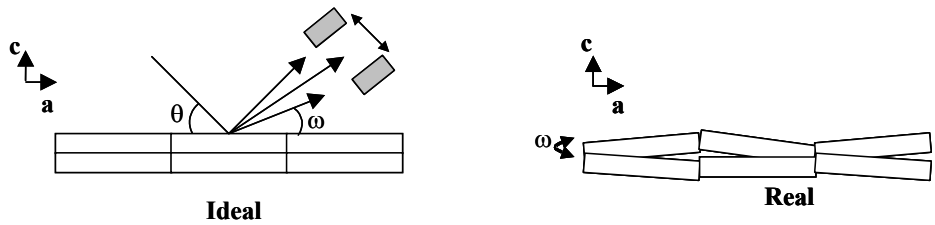

Fig. 1.23: With omega-scan is possible to evaluate how much misoriented is the sample analysed.

ϕ–scan: In ϕ–analysis is possible to appreciate the in-plane texture, to see if in the sample all the grains are oriented in the same direction respect to its surface plane (fig.1.24).

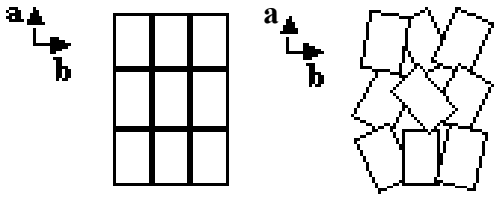

Fig. 1.24: In plane texture of a polycrystalline material.

To realize this analysis it is necessary to choose one reflection of the sample film with a relative high intensity, fix its θ value, be sure that no diffraction reflections of the substrate have the same θ and to scan the ϕ in the range from 0 to 360 degree. It is also important that the chosen reflection will be not a (h00) planes, these planes are parallel to the sample surface and are not useful to know about the in-plane texture (no diffraction reflections could be detected).

1.6.2 SMALL ANGLE X-RAY REFLECTIVITY(XRR)

XRR measurements have been performed on a Rigaku Rotaflex RU-200BV Diffractometer, in the Icmab-Csic. It is a non-destructive and non-contact technique for thickness determination between 2-200 nm with a precision of about 1-3 Å. The method consists in monitoring the intensity of the x-ray beam reflected by a sample at grazing angles. A monochromatic x-ray beam of wavelength λ irradiates a sample with a grazing angle ω and reflected intensity at an angle 2θ is recorded. The condition of incident angle $\omega = (2\theta)/2 = \theta =$ outgoing angle is satisfied. The reflection at the surface and interface is due to the different electron densities in the different layers (films), which correspond to different reflective indexes in the classical optics. For incident angles θ below a critical angle θ_c, total external reflection occurs. Above θ_c the reflections from the different interfaces interfere and give rise to interference fringes.

The period of the interference fringes and the fall in the intensity are related to the thickness and the roughness of the layer, (layers in the case of multilayer).

The formula to calculate the thickness can be simplified to:

$$d=\lambda/\ \Delta(2\theta^{o})$$

Where d is the film thickness, λ is the x-ray wavelength and $\Delta(2\theta^{o})$ is the angular distance between two consecutive peaks or valley of the interference fringes.

1.6.3 SECONDARY ELECTRON MICROSCOPY (SEM)

In this particular work we used the scanning electron microscopy (SEM) by JEOL 6300 instrument of the "Servei de Micróscopia Electrónica " at the University Autonoma of Barcelona, UAB.

This type of electron microscope is capable to produce high resolution images of a sample surface. In typical SEM configuration, electrons are thermionically emitted from a tungsten or LaB_6 cathode filament towards an anode. The electron beam, with a typical energy ranging from few keV to 50 keV, is focused by successive lenses in a beam with a very fine spot size (~5nm). The samples, if non-conductors, have to be previously covered by gold or graphite, to generate an earth contact. When the beam impact with the surface, different kind of electrons can be detected. We used the following analysis:

- **Detection of secondary electrons:** The secondary electrons come from the near surface region of the sample device. Low energy secondary electrons are generated by the inelastic interaction of the electrons beam and the surface sample electrons.

- **Micro-analysis by X-ray (EDX):** When the beam impact with the surface, some electrons jump in a higher energy level. In the relaxation of these electrons, a radiation typical of each atom is emitted**.** The part of radiation that is in the X-ray spectra is detected by a sensor and represented in a monitor. It is

possible to make a quantification of the material composition with a low sensibility.

1.6.4 X-RAY PHOTOELECTRON SPECTROSCOPY (XPS)

X-ray photoelectron spectroscopy works by irradiating a sample material with mono- energetic soft X-ray causing electrons to be ejected (fig. 1.25).

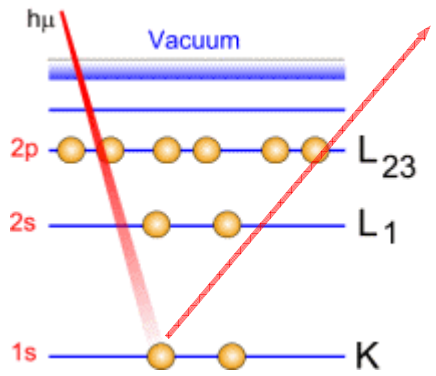

Fig. 1.25: The principle of the XPS analysis.

Consequently, surface atomic elements in the sample can be identified directly from the kinetics energies of these ejected photoelectrons. The relative concentration of elements can be determined from the photoelectron intensities. In XPS the photon is absorbed by an atom in a molecule or solid, leading to ionisation and the emission of a core (inner shell) electron. The energy of the photon (X-ray) is expressed by Einstein relation : $E=h\upsilon$

h is the Plank's constant ($6.62*10^{-34}$ Js) and υ the frequency (Hz) of the radiation. The kinetic energy distribution of the emitted photoelectron can be measured with any appropriate energy analyser; and a photoelectron spectrum can thus be recorded.

We used XPS analysis to determine the bonding state (molecular environment) and/or oxidation state of cerium in CeO_2 thin film.

1.6.5 REFLECTION HIGH ENERGY ELECTRON DIFFRACTION (RHEED)

The RHEED measures presented in this work have been performed at the Götinghen University. The geometry of RHEED is quite simple, see fig. 1.26. An accelerated electron beam (5-100 keV) is incident on the surface with a glancing angle (<3º) is reflected.

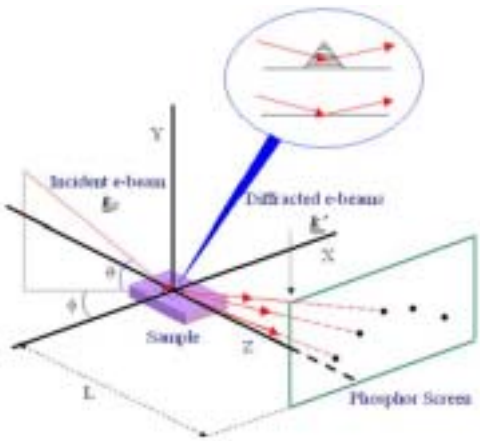

Fig. 1.26: Reflection high-energy electron diffraction RHEED analysis.

The electrons have high energy nevertheless, due to the incident glancing angle, penetrate only in the material surface. This is the reason of the high surface sensitivity of RHEED. Upon reflection, electrons diffract, forming a diffraction pattern that depends on the structure and the morphology of the probed surface. Diffraction results when the LAUE condition is satisfied: $\mathbf{k^I - k_0 = G}$.

Where k^I and k_0 are the wave vectors for the diffracted and incident beams respectively, and G is the reciprocal-lattice vector.

Reflection diffraction pattern consists of spots (or streaks) that lie on arcs (the Laue rings). When the surface has more than one domain (i.e., randomly oriented crystals), the RHEED image will be the sum of diffraction from all the different regions.

This gives rise to a system of concentric rings.

1.6.6 ATOMIC FORCE MICROSCOPY (AFM)

In our analysis we used a SCIEN TEC PicoSPM microscope from Molecular Imaging .The principle of the Atomic Force Microscopy (AFM), is the interaction (force) between a sharp tip (apex radius ~20nm) formed on a soft cantilever and sample surface (see fig. 1.27). The interaction is probed through the deflection of the cantilever.

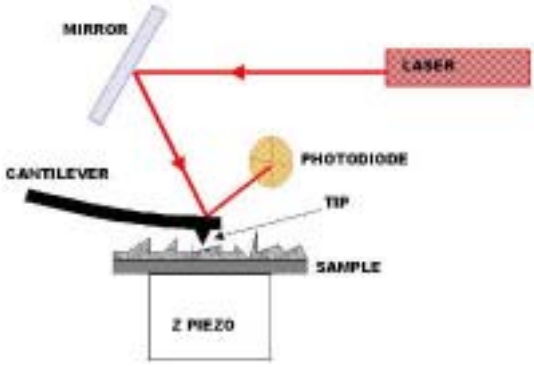

Fig. 1.27: The AFM tip is formed on a cantilever. Its movements are controlled by a laser beam.

This method permits to observe sample at nanometric scale and to measure the roughness of the sample surface. The analysis could be done in the air and is non destructive for the sample. The AFM can works in different modes but we used only the tapping mode:

Tapping mode: In this mode, a micro-cantilever is forced sinusoidally thus inducing a periodic oscillation of the cantilever. The sample properties are inferred by analysing the changes in the cantilever's oscillations due to the interaction between the sample and the cantilever tip. The difference with non-contact mode is the frequency of oscillation that is under the resonant frequency of the cantilever. In this mode the tip can touch physically the sample surface.

1.6.7 INFRARED ANALYSIS (IR)

For the Infrared Analysis IR measures we used a Perkin Elmer "Spectrum one" transmission mode of " Nanociència Molecular I Materials Orgànics" department of the Icmab-Csic of Barcelona.

For any given molecular bond, there are several specific frequencies at which it can vibrate. According to quantum mechanics, these frequencies correspond to group state (lowest frequency/energy state) and several exited states (higher frequency/energy state). One way to cause the frequency of a molecular vibration to increase is to excite the bond by having it absorb light energy. For any given transition between two states the light energy (determined by wavelength) must exactly equal the difference in the energy between the two states (usually ground state (E_0) and the first excited state (E_1).
Difference in Energy state = Energy of light absorbed

$$\mathbf{E_1 - E_0 = hc/\lambda}$$

Where h= Planks constant

c= Speed of light

λ=Wavelength of the laser

The energy corresponding to these transitions between molecular vibrational states is generally 1-10 Kilocalories/mole (200-3600 cm^{-1}), which corresponds to the infrared portion of electromagnetic spectrum. This technique is not destructive.

1.6.8 INTERFEROMETRY

The interferometer measures the interference pattern created by reflected white light from the surface of the sample. Usually it is used to measure the roughness of the material surface. The measurement is non-contact and rapid. In our study we used a Zygo apparatus to control the samples thickness thanks to the different reflection indexes of material and substrate.

REFERENCES

[1]H.K.Omnes, *Commun. Phys. Lab. Univ. Leiden* ***124****c (1911).*

[2] K.A. Müller and J.G. Bednorz, *Z. Phys. B,* ***64,*** *189 (1986).*

[3] S.N.Putilin, E.V.Antipov, O.Chmaissem, and M.Marezio, *Nature,* ***362,*** *226 (1993).*

[4] W.Meissner and R. Ochsenfeld, *Naturwissenschaften,* ***21,*** *787 (1933).*

[5] L.D. Landau and V.L. Ginzburg, *Zh. Eksp. Teor. Fiz,* ***20****, 1064 (1950).*

[6] J.Bardeen, L.N.Cooper, and J.R.Schrieffer, *Physical Review,* ***108****, 1175, (1957).*

[7] R.L. Greene, P.M. Grant, and G.B.Street, *Phys. Rev. Lett.,* ***34****, 89 (1975).*

[8] M. K. Wu, J. R. Ashburn, C. J. Torng, P. H. Hor, R. L. Meng, L. Gao, Z. J. Huang, Y. Q. Wang, and C. W. Chu, *Phys. Rev. Lett.,* ***58****, 908-910, (1987).*

[9] D. Larbalestier, A. Gurevich, D. M. Feldmann and A. Polyanskii, *Nature,* ***414****, 368-377 (2001).*

[10] D. Larbalestier, D. C. et al. *Power Applications of superconductivity in Japan and Germany (World technology and Engineering Center, Loyola College, MD, September 1997).*

[11] M.Wilson *Superconducting Magnets (Clarendon, Oxford) (1983).*

[12] A.Usoskin, J.Dzick, A.Issaev, J.Knoke, F.GarciaMoreno,K.Sturm and H.C.Freyhardt, *Supercond. Sci. Technol.,* ***14****, 676 (2001).*

[13] K.Matsumoto, S.B.Kim, I.Hirabayashi, T.Watenabe, N.Uno and M.Ikeda, *Physica C,* ***330****, 150 (2000).*

[14] Y.Iijima, M.Kimura, T.Saitoh and K.Takeda *Physica C,* ***335****, 15 (2000).*

[15] Y.Iijima, K.Kakimoto, M.Kimura, K.Takeda and T.Saitoh *IEEE Trans. App. Supercond.,* ***11****, 2816 (2001).*

[16] H.Yamane, T.Hirai, K.Watanabe, N.Kobayashi, Y.Muto, M.Hasei and H.Kurosawa *J. Appl. Phys.,* ***69****, 7948 (1991).*

[17] H.Kurosaki, T.Yuasa, T.Maeda, Y.Yamada, K.Wada and I.Hirabayashi *Physica C,* ***938****, 357-360, (2001).*

[18] B.UTZ, R.Semerad, M.Bauer, W.Prusseit, P.Berberich and H.Kinder *IEEE Trans. App. Supercond.,* ***7****, 1272 (1997).*

[19] J.Knauf, R.Semerad, W.Prusseit, B.DeBoer and J.Eichemeyer *IEEE Trans. App. Supercond.,* ***11****, 2885 (2001).*

[20] M.R.Scozzafava, W.E.Rhine and M.J.Cima, *Mat. Res. Soc. Symp. Proc.,* ***169****, 393 (1990).*

[21] T.Kumagai, H.Yamasaki, K.Endo, T.Manabe, H.Niino, T.Tsunoda, W.Kondo and S.Mizuta, *Japan. J. Appl. Phys.* ***32****, L1602 (1993).*

[22] T.Manaba, I.Yamaguchi, S.Nakamura, W.Kondo, T.Kumagai and S.Mizuta, *J. Mater.Res. ,* ***10****, 1635 (1995).*

[23] *J.A.Smith, M.J.Cima and N.Sonnenberg, IEEE Trans. App. Supercond.,* ***9****, 1531 (1999).*

[24] A.Goyal et al. Texture formation and grain boundary network in rolling assested biaxially textured substrates and in epitaxial YBCO films. *Micron,* ***30****, 463-478 (1999).*

[25] K.Matsumoto, Y.Niiori, I.Hirabayashi, N.Koshizuka, T.Watanabe, Y.Tanaka, M.Ikeda, in: K.Osamura, I.Hirabayashi (Eds.), *Advansces in Superconductivity X 611-614 (1998).*

[26] K.Matsumoto, S.B.Kim, J.G.Wen, I.Hirabayashi, T.Watanabe, N.Uno, M.Ikeda, *IEEE Trans. App. Supercond.,* ***9****, 1539 (1999).*

[27] Y.Iijima, K.Kakimoto, M.Kimura, K.Takeda, K.&T.Saitoh, Reel to reel continuos formation of Y-123 coated conductors by IBAD and PLD method., *IEEE Trans. App. Supercond.,* ***11****, 2816-2821 (2001).*

[28] C.J.Brinker and G.W.Scherer, SOL-GEL Science : The physics and Chemestry of SOL-GEL Processing (Academic Press, Inc. New York, 1990).

[29] http://www.unifr.ch/physics/mm/proj/coll_solgeltran.html

[30] R.W.Schwartz, *Chem.Mater.,* ***9****, 2325-2340, (1997).*

[31] K.D.Budd, S.K.Dey, D.A.Payne, *Brit.Ceram.Soc.Proc.,* ***36****, 107, (1985).*

[32] S.K.Dey, K.D.Budd, D.A.Payne, *IEEE Trans.UFFC,* ***35****, 80, (1988).*

[33] P.K.Coffman, S.K.Dey, *J.Sol-Gel Sci.Technol.,* ***251****, 1, (1994).*

[34] R.W.Schwartz, R.A.Assink, T.Headley, *J.Mater.Res.Soc.Symp.Proc.,* ***243****, 245, (1992).*

[35] G.Yi, Z.Wu, M.Sayer, *J.Mater.Sci.,* ***64****, 2717, (1988).*

[36] Y.Takahashi, et.al., *J.Mater.Sci.,* ***25****, 3960, (1990).*

[37] R.W.Vest, J.Xu, *IEEE Trans.UFFC,* ***35****, 711, (1988).*

[38] G.H.Heartling, *Ferroelectrics,* ***21****, 119, (1991).*

[39] Y.Ito, et. Al., *Int.Ferro,* ***14****, 123, (1997).*

[40] M.F.Ng, M.Cima, *J.Mater.Res.Soc.Symp.Proc.*, ***341***, *145, (1994).*

[41] S.Doeuff, Y.Dromzee, C.Sánchez, *C.R.Acad.Sci.Paris,* ***308****,1409, (1989).*

[42] T.M.Alam, T.J. Boyle, C.D.Buchheit, R.W.Schwartz, J.W.Ziller, *Mater.Res.Symp.Proc.,* ***346,*** *35, (1994).*

[43] http://www.mse.arizona.edu/faculty/birnie/Coatings/Defects.htm

[44] C.Teichert, *Physics Reports,* ***365****, 335-432, (2002).*

[45] J.E.Shelby,*Introduction to Glass Science and technology, 2nd ed.,Springer, (2005).*

[46] R.J.Roy, *J.Am.Ceram.Soc.,* ***52****, 344, (1969).*

Chapter 2

IMPORTANCE OF THE STUDY OF CSD BUFFER LAYERS FOR THE OPTIMISATION OF COATED CONDUCTOR ARCHITECTURES

2.1 INTRODUCTION

The role of buffer layers in heteroepitaxial systems is twofold. First, they must transmit the desired orientation to the film, and secondly, they must act as diffusion barriers against oxygen and cation diffusion. Low oxygen diffusion coefficients are important to prevent the oxidation of metallic substrates, like Ni or Cu, while cation diffusion is specially important to avoid undesired doping of the YBCO film. In order to satisfy the first requirement, buffer layers must grow epitaxially on the substrate, which imposes a constraint on the lattice parameters in such a way that the buffer layer material must exhibit matching distances on the free surface of the substrate. Moreover, the buffer layer must cover homogeneously the surface of the underlying substrate. As reviewed by Palstrom [1], the main issues governing the epitaxy between two dissimilar materials can be summarised as follows:

1) The mismatch must be as small as possible.
2) Chemical bonding across the interface must be compatible with the desired alignment between both crystal lattices.
3) The buffer material must completely wet the underlying substrate, which from a thermodynamic standpoint requires that the surface energy of the growing layer γ_f plus the interface energy per unit area γ_i must be lower than the substrate surface energy per unit area γ_s (i.e. $\gamma_f+\gamma_i<\gamma_s$), (see chapter 1. pag.22).
4) Under the employed processing conditions, the heteroepitaxial system must be thermodynamically stable in the sense that no reaction should take place between adjacent layers.

Obviously, since the buffer layer must in turn accommodate subsequent buffer layers or the YBCO layer itself, the above requirements must apply for all the different layers composing the system while the condition of low surface roughness (5) is to be added to the list.

Not all the above conditions are exclusively compound dependent but many issues are to be controlled through processing. Thus, only point (1) and oxygen/cation diffusivities are to be satisfied through a proper selection of the buffer layer compound.

Other issues such as the phase stability requirements quoted in point (4) are to be tackled through analysis of the phase diagram. As argued by Palstrom [1], even wetting effects can be tuned through the kinetics of the growth process.

In practice, owing to the unavailability of relevant quantities along with the tremendous complexity of the epitaxial growth mechanism of multicomponent oxides, the search for adequate buffer layers follows a trial-and-error procedure in which the unique selection criteria is the lattice mismatch. Fortunately, however, lattice matching appears to be the most important parameter in controlling the epitaxy.

2.2 AIMS AND STRATEGY

This particular work has its “core” objective in the synthesis of YBCO by TFA method on a template consisting of a metal substrate and a top CSD-buffer layer system, with a minimum critical current density of 1 MA/cm^2 at 77K.
To achieve this aim we divided this experimental work in three main parts:

1. The first approach will be the study of the growth parameters for different buffer layers on single crystals. The choice of the single crystals for preliminary tests will be restricted to those materials with similar crystallographic parameters and structure to the template oxide layers candidates for the superconducting cables. For example, to simulate the behaviour of the NiO(SOE) substrate, the MgO single crystal is a useful substitute because it has near by the same lattice parameter (cubic a_{MgO}=

4.21A a_{NiO}=4.18 A) and the same crystallographic structure. As the single crystal is a simpler system than the textured polycrystalline material, it will be easier to define the optimum growth parameters.

2. Next step will be adapting the CSD optimised process to grow the buffer layers on the metal substrates. In particular the YSZ(IBAD)/Stainless Steel (YSZ(IBAD)/SS) from Göttingen university, and NiO(SOE)/Nickel(RABiT), from Cambridge university will be used. It is evident, for example, that using the stainless steel as metal substrate, it will be important to adjust the growth parameters to avoid its oxidation.

3. The last part of this research will be focused on testing the TFA-method, experimentally developed in our laboratories by Oscar Castanyo [2], to grow YBCO superconductor on the optimised buffer layers. Critical currents will define the real quality of the final superconductor. The YBCO coated conductors grown on single crystals will fix the upper limit of the superconducting performances obtainable on metal technical substrates.

2.3 TECHNICAL METAL SUBSTRATES

The NiO(SOE) substrates were produced by the IRC department of superconductivity and Material Science department of the Cambridge University [3].

Previously, the Nickel treated for controlled oxidation, had been textured in a RABiT process (Rolling Assisted Biaxial Texturing) in the institute IFW of Dresden[4].

The cube textured Nickel or Ni-based alloy tapes are prepared by heavy cold rolling and subsequent annealing in a controlled Ar/H_2 atmosphere (fig. 2.1). The optimum texturing conditions for the Ni, such as annealing temperature and time of recrystallization are closely dependent on the Ni purity and the content microalloying elements such as Mo or Mn which stabilise the structure and shift the temperature of the secondary recrystallization.

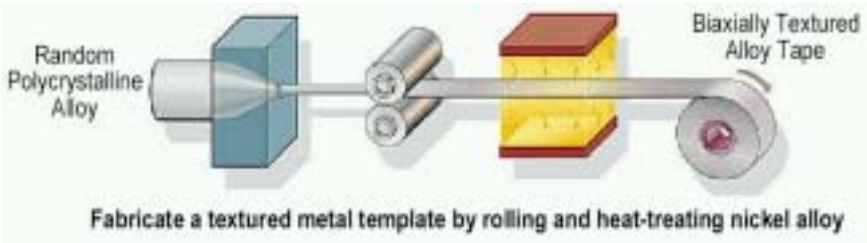

Fig. 2.1: Preparation process of the Ni(RABiT) substrates.

Nevertheless it is known that the Nickel(RABiT) is as well a good substrate for the deposition of epitaxial oxides, such as CeO_2 or MgO which act as oxygen barrier against uncontrolled oxidation of the Ni. Depending on the deposition conditions, CeO_2 and MgO buffer layers are not always effective to avoid this kind of oxidation [5] that could impede the correct transfer of biaxial texture from the substrate to the final YBCO thin film. The alternative approach is the controlled oxidation of the nickel surface by self oxidation epitaxy (SOE).

The process consists of the control of the NiO(SOE) nucleation and growth at high temperature where the (00l) orientation is favoured. Since the oxidation in the early processing stages produces NiO(SOE) with (111) and (220) preferred orientations, a reducing atmosphere of Ar-Ar/ H_2 5% is employed till reaching the optimum range of temperatures, between 950ºC-1300ºC. The furnace atmosphere is then switched to air or Ar/O_2 [3].

Under optimised conditions NiO(SOE) films are obtained with an out-of-plane full width at half maximum (FWHM) of about 3º and an in-plane FWHM of 5º. These values demonstrate a high biaxial texture especially taking into account that Nickel is a polycrystalline metal and not a single crystal.

One alternative to Ni(RABiT) or NiO(SOE) is the biaxially textured yttria-stabilized zirconia (YSZ) films grown by ion-beam-assisted deposition (IBAD) on stainless steal.

YSZ(IBAD) substrates on stainless steel have been supplied by Göthinghen University [6]. The IBAD system employs two ion sources of sputtering as shown in fig. 2.2.

The YSZ target is sputtered by a Xe source while the second ion beam of Ar impinging the growing film is at a fixed angle of 55º from the perpendicular direction to the substrate.

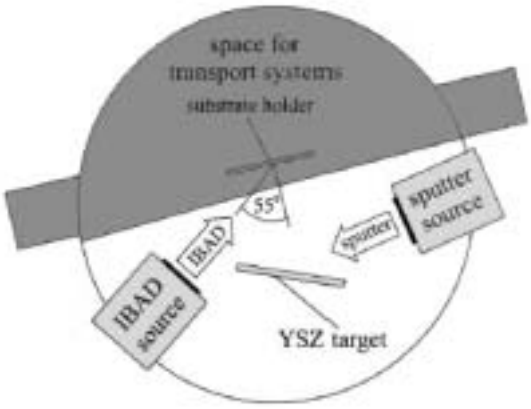

Fig. 2.2: Ion beam deposition process of the YSZ(IBAD)/SS substrates. An Ar^+ beam is positioned at 55º with respect the normal direction to the substrate surface to re-sputter the grains that grow with undesired orientations [6].

An oxygen partial pressure of $1{\cdot}10^{-4}$ mbar was maintained to ensure full oxidation of the film. In the first stage of the YSZ growth (0-50 nm), (011)-oriented grains nucleate, till a middle stage (50-100nm) where while the (011) grains continue to grow, (001) grains nucleate showing a preferential in plane alignment. In the final growth stage (> 100 nm), the second beam (Ar one) that till the moment has generated compressive stress into the material, etches the (011) and the (001) misaligned grains.

The (001)-oriented grains with their ⟨111⟩ axis parallel to the assisting ion beam do have a lower etching rate thus favouring their growth. The in-plane texture of the YSZ improves with the film thickness; optimising the process is possible to reach a value of out-of- plane FWHM 4º and in-plane FWHM of 7º [7].

2.4 THE PROPER BUFFER LAYER ARQUITECTURE

Epitaxy is the most important phenomenon in thin film device technology. It is a way of growing a crystal layer of one material on a crystal surface of another crystal in such a way that its crystalline orientation is the same as that of the substrate.

There are two main types of epitaxy, the homoepitaxy refers to the growth of a film on a substrate made of the same material, and the heteroepitaxy where films and

substrate are composed of different materials. Heteroepitaxy is the more common phenomenon and the one we are mainly using in our research. Depending on the degree of matching and the thickness of the film it is possible to distinguish three regimes: Matched, Strained and Relaxed [8], (fig. 2.3).

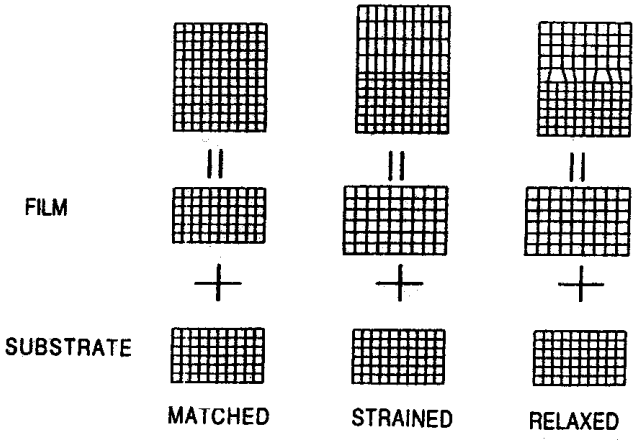

Fig. 2.3: Schematic illustration of lattice-matched, strained, and relaxed heteroepitaxial structures.

Small lattice mismatch is normally desired and the best situation to obtain a film free of defects. When the mismatch increases also the film strain does. Strained-layer epitaxy generally prevails in the first stage of material growth irrespective of the crystal structure or mismatch in lattice parameters. Increasing the film thickness above a critical value, the strained layer relaxes via interfacial dislocations. The lattice mismatch ε, for tetragonal, pseudocubic and cubic materials can be expressed as [9]:

$$\varepsilon(\%) = \frac{a_f - a_s}{a_f} \cdot 100$$

A positive mismatch indicates that the film is under compressive strains, negative on the contrary, that the strains are tensile. As explained in chapter 1, the smaller the mismatch the smaller will be the wetting angle that forms the film with the substrate and nucleation on the substrate will be more favourable.

It is then essential to plan the coated conductor architecture considering that the buffer between metal substrate and the YBCO has to match as better as possible with both materials. In fig. 2.4 the red points represent the matching distance of the typical buffer layers with the YBCO superconductor.

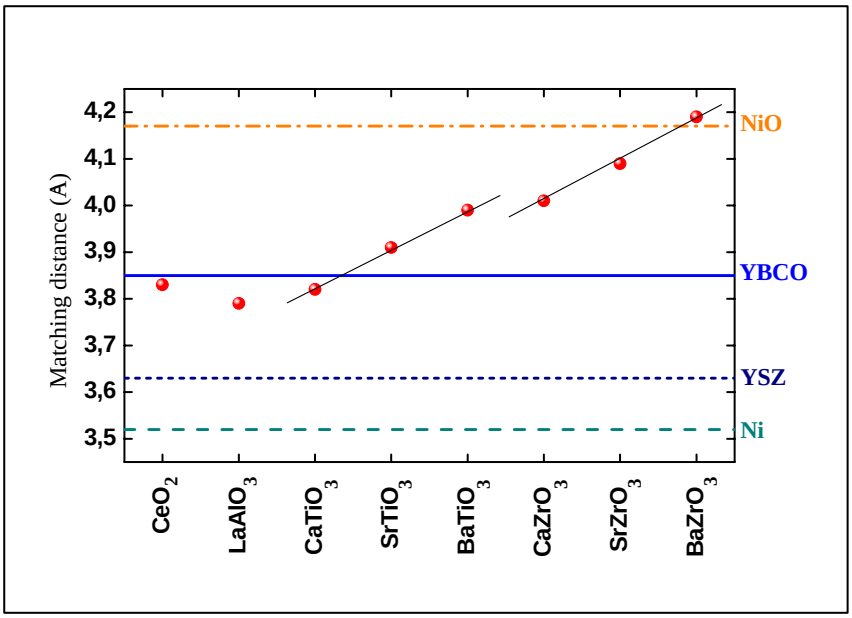

Fig. 2.4: Calculated mismatch of different buffer layers with respect to the YBCO cell parameter.

The first four buffers from the left, CeO_2, $LaAlO_3$, $CaTiO_3$ and $SrTiO_3$ have the better match with the YBCO, nevertheless it is necessary to take into account also the cell parameters of the substrates. As said before the technical metal substrates we have employed are NiO(SOE)/Ni and YSZ(IBAD)/SS.

TABLE 2.1: Mismatch values of buffer layers with respect the two metal substrates available, YSZ(IBAD)/SS and NiO(SOE)/Ni(RABiT).

BUFFERS SUBSTRATE	**CeO2** *a=5,411*	**LaAlO3** **a=3,79** **a √2=5,35**	**BaZrO3** *a=4.193* **a √2=5,93**	**SrTiO3** **a=3.905** **a √2=5,52**
YSZ/SS **a=5.139**	+5 %	-	-22.6% +13.3% (diag.)	-
NiO(SOE)/Ni **a=4,177** **a √2=5,91**	-	-	+0.38%	-7%

In table 2.1 the cell parameters of the metal substrates and some of the possible buffer layers are presented. Mismatch values are calculated on the basis of the more favourable epitaxial relation. The buffer grows cube on cube or on the diagonal relative to the substrate ([100]s//[100]f or [100]s//[110]f), (fig.2.5(a,b)).

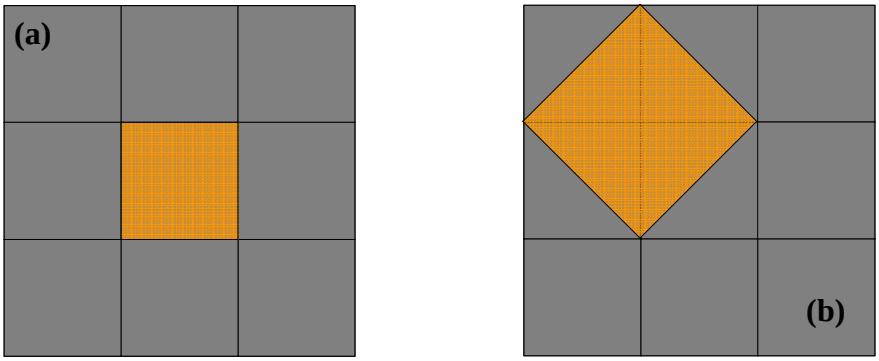

Fig. 2.5(a,b): Typically observed epitaxial relationships. Cube on cube (a), and diagonal (b).

Besides the possibilities presented above, it is also possible an architecture composed by two different buffer layers where the mismatch changes more gradually form the substrate to the YBCO. In the case of NiO, $BaZrO_3$ (BZO) matches perfectly but not in the same way with the YBCO film. Intercalating between NiO and YBCO, first the BZO and then a $SrTiO_3$ (STO) buffer layer the mismatching will vary as NiO-BZO 0.38%,BZO-STO -7.38%, to STO-YBCO -1.24%, in spite of BZO-YBCO +0.38%, -8.7%.

In these purely crystallographic considerations we have not taken into account any effect of the chemical affinity between substrate and film that could strongly influence its growth.

In this particular work we focused especially on the CeO_2 buffer layer on YSZ substrates and STO on NiO. Other options as the double buffer BZO/STO on both kinds of substrates have also been explored.

REFERENCES

[1] C. J. Palmstrom, *Annu. Rev. Mater. Sci.*, ***25***, *389 (1995).*

[2] O.Castanyo PhD Thesis (2004).

[3] A.Kursumovic,R.Hühne, R.Tomov, B.Holzapfel, B.A.Glowacki, J.E.Evetts. *Physica C,* ***405,*** *219-226, (2004).*

[4] B.Boer, N.Reger, L.Fernandez, J.Eickemeyer, B.Holzapfel, L.Schultz, W.Prusseit, P.Berberich, *Physica C,* ***351****, 38-41, (2001).*

[5] T.J.Jackson, B.A.Glowacki, J.E.Evetts, *Physica C,* ***296****, 215-224, (1998).*

[6] J.Dzick, J.Hoffmann, S.Seviers, L.O.Kautschor, H.C. Freyhardt. *Physica C,* ***372-376,*** *723-728, (2002).*

[7] J.Wiesmann, J.Dzick, J.Hoffmann, K.Heinemann, H.C.Freyhardt, *App. Supercond.,* ***1-2****, 997-1000, (1997).*

[8] L.B.Freund and S.Suresh, *Thin film materials,Cambridge University Press, (2003).*

[9] P.A.Langjahr, F.F.Lange, T.Wagner, and M.Rühle, *Acta Mater.,* ***46****, 773-785, (1998).*

Chapter 3

GROWTH OF CeO_2 BUFFER LAYERS BY MOD

In this Chapter a first approach to the optimisation of the synthesis parameters is presented. An investigation of the growth mechanism has been carried out in order to understand an unexpected behaviour of cerium oxide, consequently is presented in the next Chapter.

3.1 SYNTHESIS AND GROWTH OF CeO_2 FILMS ON (001)-YSZ SINGLE CRYSTALS

The first tests to optimise the synthesis of cerium oxide buffer layers, have been performed on 5mm X 5mm X 0.5mm (001)-YSZ single crystal substrates supplied by Crystec. The characteristic topographical features are R_a = 0,193 nm, RMS = 0,266 nm, and P-V = 2,65 nm, where R_a : average roughness, is the arithmetic mean of the deviations in height from the image mean value:

$$R_a = \frac{1}{N}\sum_{i=1}^{N}\left|Z_i - \overline{Z}\right|$$

RMS : root-mean-square-roughness, is defined as the square root of the mean value of the squares of the distances of the points from the image mean value:

$$RMS = \sqrt{\frac{1}{N}\sum_{i=1}^{N}\left(Z_i - \overline{Z}\right)^2}$$

and P-V : maximum peak-to-valley range in the analysed area.

On the other hand, the technical metal substrates used were produced in the University of Göttingen. They consist of a (001)-YSZ template deposited by Ion-Beam-Assisted-Deposition (IBAD) on Stainless Steel (SS) henceforward referred to as YSZ(IBAD)/SS. As received substrates were cut with scissors into 5 mm x 5 mm x 0.5 mm pieces.

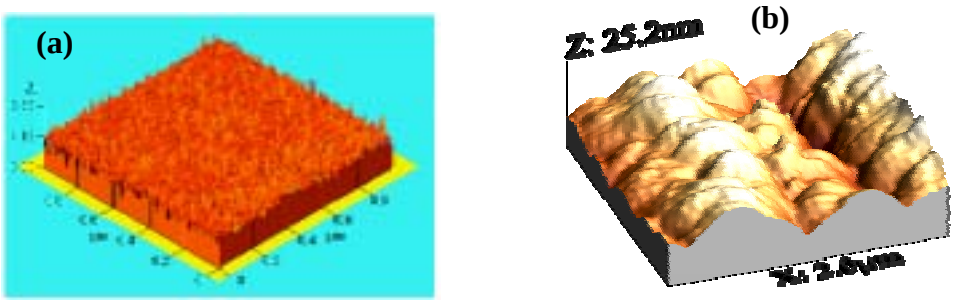

Figs. 3.1(a,b): (a) AFM analysis by 1·1μm scan of YSZ single crystal. (b) 2·2μ scan of YSZ(IBAD)/SS tape.

Figs. 3.1 (a) and (b) show AFM images of the (001) surface of a YSZ single crystal and a IBAD deposited YSZ template, respectively. The smaller roughness and higher morphological homogeneity of the single crystal is apparent. In addition, the (001)-YSZ(IBAD) surfaces typically exhibit grooving along the axis of the tape resulting from the Ar ion bombardment. Such parallel and straight grooves are clearly observed in the SEM image shown in fig. 3.2, and in the AFM image shown in fig. 3.1(b).

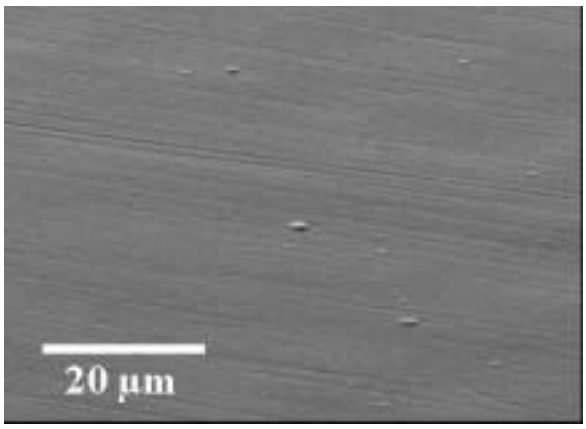

Fig.3.2 : SEM image of YSZ(IBAD)/SS substrate. The sample looks like quite homogeneous. The visible rays are due to the IBAD technique used for the YSZ deposition.

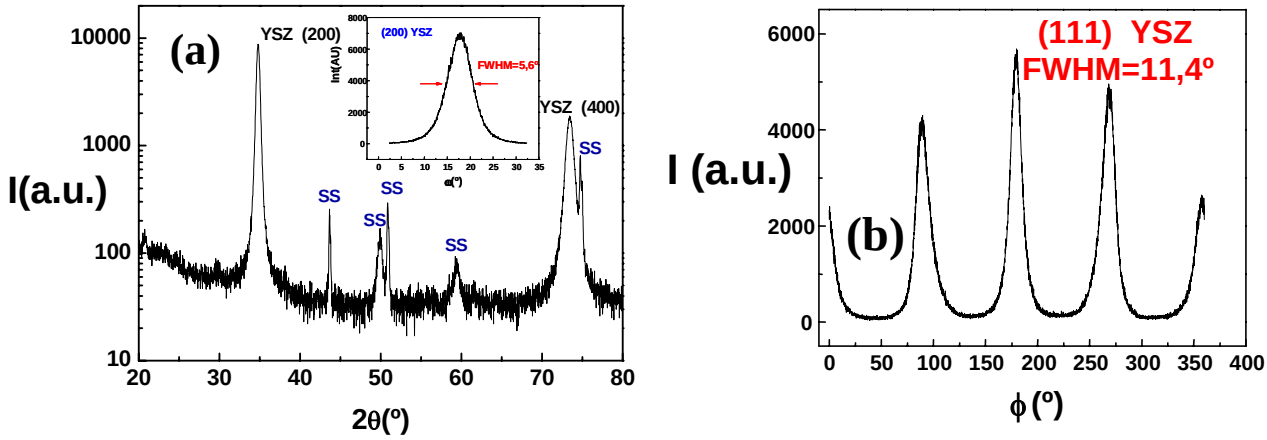

Fig. 3.3 (a,b): (a) shows a θ/2θ pattern of the YSZ(IBAD)/SS tape. Only the (00l) peaks of YSZ are present. The stainless steel peaks are marked by SS. Inset shows the (200) rocking curve of YSZ, exhibiting FWHM of 5.6º. (b) is a (111) ϕ-scan revealing four peaks 90º apart with FWHM of 11.4º.

XRD patterns of IBAD deposited YSZ templates typically present only (00l) type reflections, thus revealing a unique crystallographic orientation (fig. 3.3 (a)). The off-plane texture given by the rocking curve is Δω~6º (fig. 3.3 (a)). (111) ϕ-scans only reveal four peaks, indicating a unique in-plane epitaxial orientation, with a misorientation spread of ~11º (fig. 3.3 (b)).

The main morphological and structural features of the YSZ^{SC} and YSZ(IBAD)/SS substrates employed in the present work are listed in Table 3.1.

TABLE 3.1: Comparison between the texture and the roughness values of the YSZ single crystal and YSZ(IBAD)/SS tapes.

	Δω	Δϕ	Rms(nm)	P-V(nm)
YSZ^{SC} (single crystal)	0.1º	0.12º	0.26	2.65
YSZ(IBAD)/SS (tape)	5.6°	11.4°	4.5	25
YSZ(IBAD)/SS (tape) Best batch	5º	9.5º	5	20

3.2 PRECURSOR SOLUTIONS AND DEPOSITION PARAMETERS

3.2.1 PREPARATION OF PRECURSOR SOLUTIONS

Before choosing the better CSD route, we tested different cerium precursors in different solvents with different polymerisation agents, see Table 3.2.

TABLE 3.2: Different CSD routes investigated in the present work.

ROUTE	CE(III) PRECURSOR	SOLVENT	POLYMERISATION AGENT	CATALYST CATALIZATOR
1	Ce (III) Acetate	Water	Etilen glycol	Citric Acid
2	Ce (III) Acetate	2-Propanol	Tartaric Acid	Acetic Acid
3	Ce (III) Acetate	Water	EDTA and UREA	Nitric Acid
4	Ce(III) 2,4-Acetylacetonate	Glacial Acetic Acid	-	Nitric Acid
5	Ce(III) Nitrate	Water	EDTA ,UREA , SPAN-20, OIL OF VASELLINA	Nitric Acid

The lack of bibliography on the cerium oxide growth by CSD brought us to discard different solutions only on the basis of the XRD results. After the preliminary tests, the acetylacetonate method, number four in the table, permitted the epitaxial growth of the CeO_2 buffer layers. Owing to its easy preparation and reproducibility was then selected.

Precursor solutions were prepared by dissolving a weighted amount of cerium(III) acetylacetonate hydrate (Alfa Aesar, 99.9%) in 2 ml of Glacial Acid Acetic (Panreac).

The mixture was stirred for 15 minutes at 40ºC on a hot plate. A yellow and transparent solution was obtained (fig.3.4 (a)).The life time of the solution was of several hours after which white precipitates were found to nucleate, (fig. 3.4 (b)).

Fig 3.4 (a,b): In (a) the precursor solution is recently prepared, yellow and transparent; (b) after several hours precipitates appear at the bottom of the bottle.

A sample of precipitates was washed with acetic acid , dried in an oven at 100ºC, and dissolved in deuterium water for their analysis by [1] H-NMR (fig. 3.5).

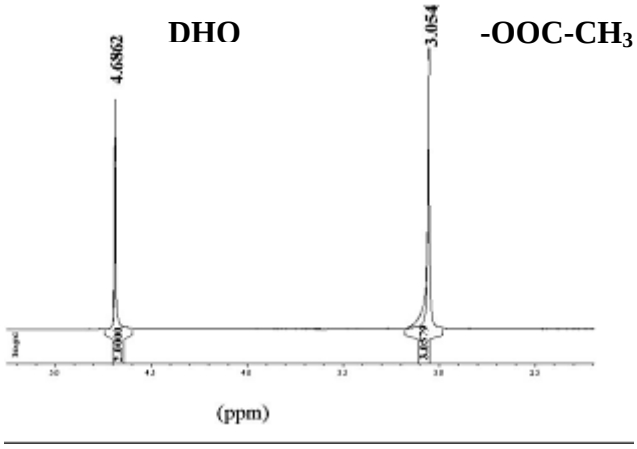

Fig. 3.5: [1] H-NMR analysis of the precipitates found in the cerium precursor solution. The analysis was performed after dissolving the precipitates by deuterium water.

Results are shown in fig. 3.5, where two peaks are clearly visible: The first at 3.06 ppm corresponds to the methil group of the acetate anion. It is shifted with respect to its normal position because of the presence of the cerium cation. The second one corresponds to the DHO compound often present when using deuterium water [1]. H-NMR analysis of commercial cerium acetate has generated the same two peak spectrum thus confirming the precipitation of acetates in the solution. To stabilise the precursor

solutions it is sufficient to add 5-25 % in volume of water or methanol just after the preparation. No visible precipitates have been found for at least one week. Probably the water or the methanol molecules co-ordinate with the cerium (III) cation stabilizes the solution, inhibiting the formation of cerium acetate.

3.2.2 VISCOSITY

To control the stability of the precursor solution we made a study of its viscosity. A Rheometer HAAKE RHEOSTRESS 600 by thermo electron (GmbH) has been used.

Usually when in a solution new chemical bonds between molecules form, or some precipitates appear due to aging phenomena, these events are associated to a change of the viscosity of the solution with time.

Viscosity is also a good way to control the thickness of the deposited film; an increase of the viscosity corresponds to an increase in thickness. In fig. 3.6 it is shown its linear dependence with the solution concentration (no stabilizing water has been added).

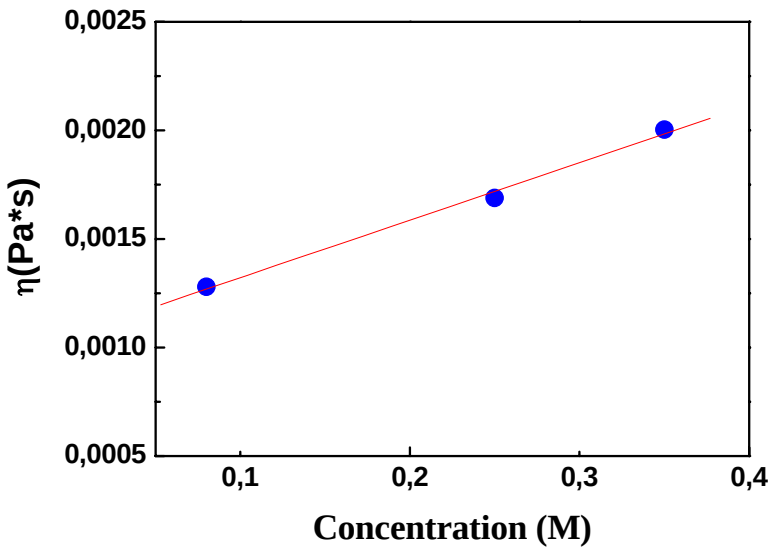

Fig. 3.6 : Linear dependence of the precursor solution concentration with the viscosity.

The viscosity is correlated to the solution concentration but also to the intrinsic nature of the solvent used; maintaining constant the concentration it is possible to

increase or decrease the viscosity only mixing different solvents. This behaviour is not always foreseeable just by knowing the viscosity of the separate solvents.

Due to the instability of the solution with time, we performed some tests adding different percentages of water and measuring the final viscosity. At the beginning we saw that increasing the amount of water the viscosity increased as well (fig. 3.7, blue squares). This could have been attributed to a chemical transformation in the precursor solution, but repeating the measurements only of the matrix (acetic acid and the same amount of water: 0%, 5%, 10%, 20%) the same trend was found (fig. 3.7, red points).

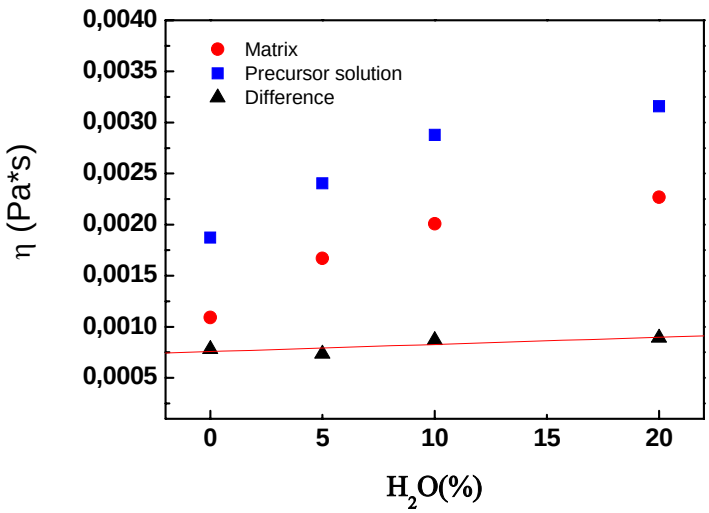

Fig. 3.7: Linear dependence of the precursor solution concentration with the viscosity.

The black triangles in fig. 3.7 are the difference in viscosity between the precursor solution with a particular amount of water and the matrix at the same concentration (fixed for all the samples at 0.25M). The values calculated in this way do not depend on the amount of water. In fact the increase in viscosity with water concentration is only due the effect of the dilution of the acetic Acid and not to formation of new chemical bonds.

Since the stability does not increase with water concentration, we decided to fix it in 5%(Vol) for a better wettability of this particular solution on the substrate (see spin coating section pag.58).

To confirm the reproducibility of this method, we studied the viscosity of three different solutions obtained at the same conditions, 0.25M in cerium acac and 5% vol.

of water, but prepared in different days (fig. 3.8).The curves showed a viscosity close to 2.5 mPa·s in the three different cases demonstrating the reproducibility of the method.

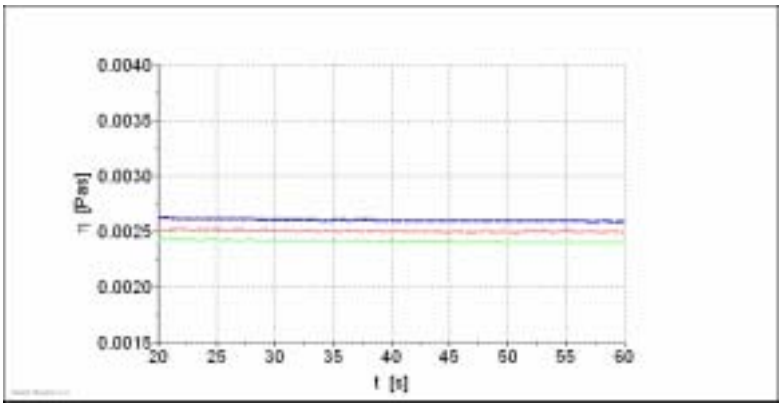

Fig. 3.8: Reproducibility study of the solution preparation method. Three solutions were prepared at the same conditions and measured with a rheometer; η~ 2.5 mPa·s.

We studied also the stability of viscosity with time (fig. 3.9). The formation of precipitates is only a macroscopic sign, and probably before they are visible to human eye small suspended particles are already present in the solution. These particles could be detected by measuring a change of viscosity. A solution of 0.45M in cerium acac stabilized by 5% in volume of water, has been measured during three days with an interval of 24h between each measurement (fig.3.9). The viscosity results to be constant (3mPa·s).

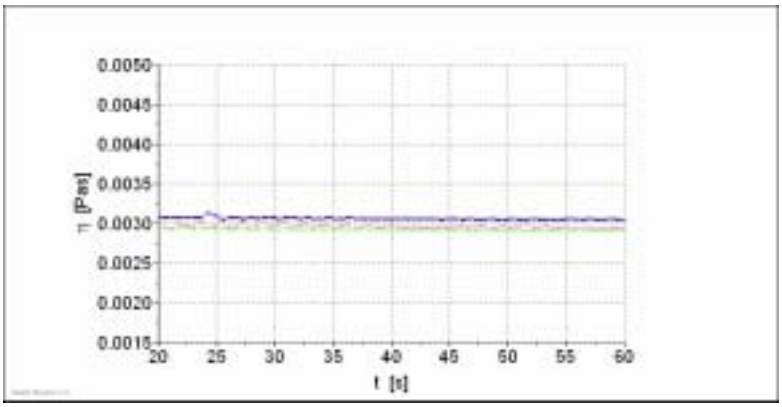

Fig. 3.9: Stability test of the viscosity of a 0.45M solution with time. The measures have been performed after solution preparation (green line), 24h (blue line) and 48h (red line).

Despite the volatility of the acetic acid, boiling point at 118°C, following a strict preparation procedure it is possible to control the viscosity of the solution with a high degree of accuracy.

Finally we analysed the effect of temperature on the viscosity. In fig. 3.10 the result for a solution of cerium acetylacetonate dissolved in acetic acid with a concentration of 0.25M, shows an inverse linear dependence of viscosity with temperature. This result makes clear the importance of controlling the substrate and solution temperature before deposition, otherwise it would be impossible to control the final thickness of the film. As explained in chapter 4, the thickness of the film results to be a fundamental factor to obtain a completely textured CeO_2 films.

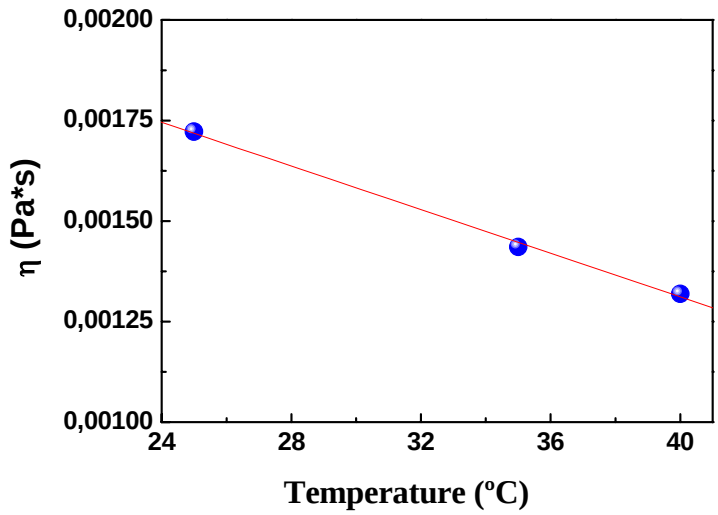

Fig. 3.10: Influence of the solution temperature on its viscosity

3.2.3 SPIN COATING

The deposition system is a commercial spin coater in which it is possible to control the acceleration and the spinning rate. Before deposition, the substrate is cleaned in an ultrasonic bath by a two step process using acetone and methanol, starting from the less polar solvent and ending with the more polar one, in order to eliminate both a-polar and ionic substances from the sample surface. Once cleaned, the substrate is fixed

on a white Teflon tap, (fig. 3.11(a,b)), with a double face scotch tape. Then, one drop of precursor solutions is deposited on top of the substrate with a syringe and the spinner is turned on.

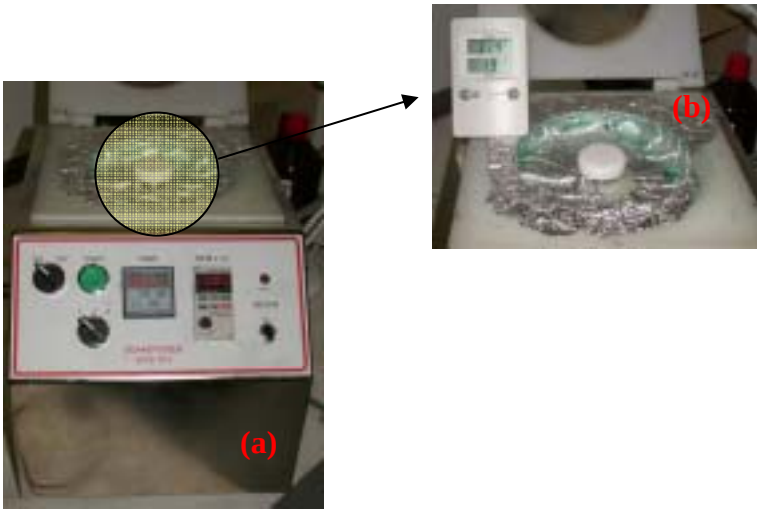

Fig. 3.11 (a,b): (a) Spin-coater apparatus. (b) Teflon tap to fix the samples.

After several tests, we found that to reach complete coverage of a 5 mm X 5 mm substrate, the optimum amount of solution is about 13 µl. The volume of the drop is controlled by a micro-syringe. Due to the acceleration, the excess of solution is expelled from the substrate and a homogeneous polymer film is formed, (fig. 3.12(a,b)).

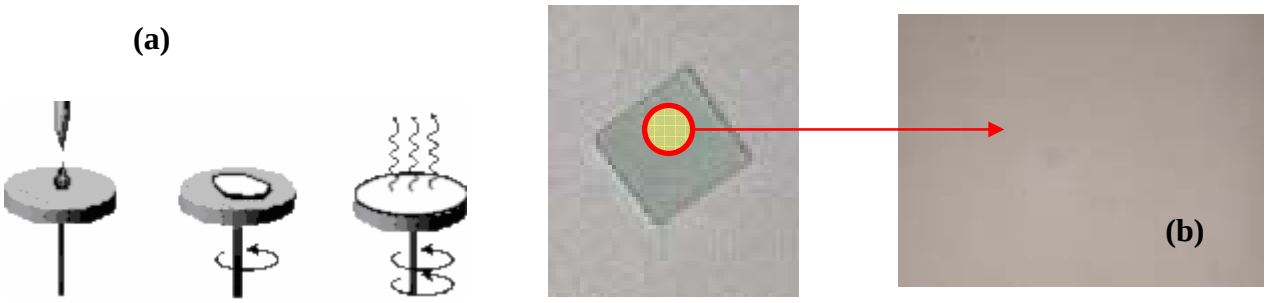

Fig. 3.12 (a,b) : (a) Gel formation during spin-coating. (b) Transparent film obtained after the spin coating process.

After the spinning step, the sample is dried under an IR lamp at about 70-80ºC for several minutes. Optimum results for this particular solution were obtained for an

acceleration of 3000 r.p.m.s^{-1} , spinning rate 6000 r.p.m. and total deposition time 2 minutes. Depending on the deposition parameters and the precursor chemical solution, it is possible to avoid some defects in the film such as striations, edge effects or swirl patterns, etc.

3.2.4 PYROLYSIS

In a first stage we adapted a thermal treatment as depicted in fig.3.13, that had been used in a similar sol-gel process for BZO [2,3]. In the first step the heating rate is of 60ºC/h up to 250ºC, while the second ramp of 200ºC/h is applied until reaching T_{max}. The whole process is carried out under a controlled flux of Ar/H_2.

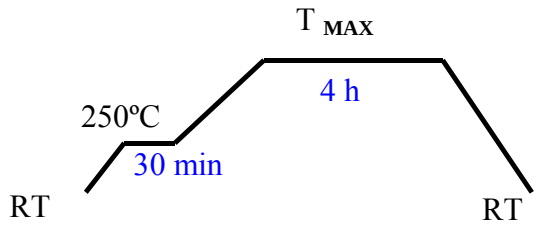

Fig. 3.13: A standard thermal treatment for the pyrolysis process.

The first step is a slow temperature ramp to avoid cracks formation during the organic part decomposition of the sol gel film. A small step is done to be sure that all the organic groups have decomposed.

In order to get insights into the pyrolisis process, the weight loss during an identical thermal treatment was analysed by TGA (Thermo Gravimetric Analysis). A sample of precursor solution dried at 100 ºC for several hours until gelification was used. Results are shown in fig.3.14.

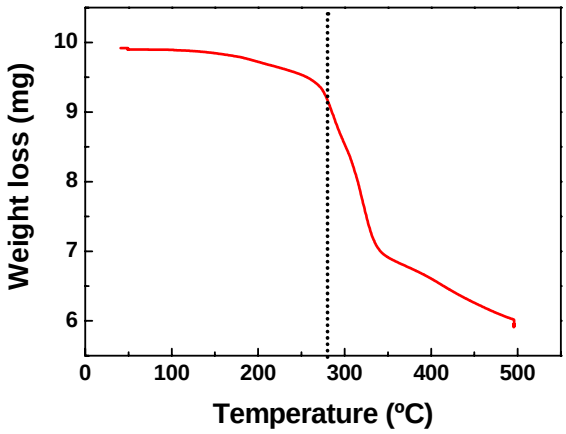

Fig. 3.14: TGA analysis of the Ce precursor solution. The organic decomposition starts near 280ºC.

The TGA result in fig.3.14 shows that the decomposition of the organic compounds at 250°C has not started. This indicates that the decomposition process takes place during the second ramp between 250°C and $\mathbf{T_{max}}$.

We have confirmed this result by another technique: IR analysis (Infrared, see chapter 1. pag.36), which is able to measure the vibrations of organic molecules directly deposited on the single crystal. It is thus possible to follow the acetylacetonate decomposition under the real experimental conditions (fig. 3.15). The acetylacetonate group is characterised by a diketone group that in IR analysis absorbs in the region of 1600-1400 cm^{-1}.

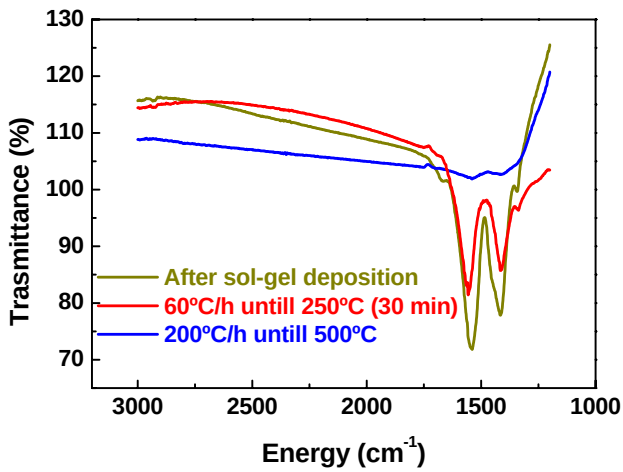

Fig. 3.15 : IR analysis of a deposited Ce MOD-film . After the standard pyrolisis (Red line), the organic film is not yet decomposed.

First we performed an IR analysis just after the deposition to recognize the acetylacetonate group at 1600-1400 cm^{-1}, the typical value reported in literature [4].

Since in the first test the signal was too weak, we increased the solution concentration up to 0.7M. After the IR analysis we treated the same sample at 250 °C for 30 minutes in Ar/H_2 as usual but this time stopping the process after the dwell at 250°C. The acetylacetonate signal did not disappear thus confirming the TGA results.

The signal disappeared only after the second treatment at 500ºC (blue curve). These results indicated that the pyrolisis could be further optimised.

One parameter of fundamental importance during precursor solution deposition, is the humidity of the atmosphere. We became aware of this fact after noting an increase of the irreproducibility of the results performed during summer. We started to measure the room temperature and the relative humidity in the spin coating room, see fig. 3.11(b). To compare different ambient conditions it's better to transform the relative humidity values in absolute ones according to the following formula:

$$Hum_{Abs} = \frac{Hum_{Rel} \cdot P_{H_2O}{}^{Sat}(T) \cdot M_{air}}{R \cdot T}$$

Where: M_{air} is the air density (g/m^3), R is the gas constant, T is the temperature in Kelvin and $P_{H2O}Sat(T)$ is the water partial pressure at temperature. Fig. 3.16 shows a collection of absolute humidity values all long the year. We found that the best moisture condition to increase the experimental reproducibility is below 10 g/m^3 (black line).

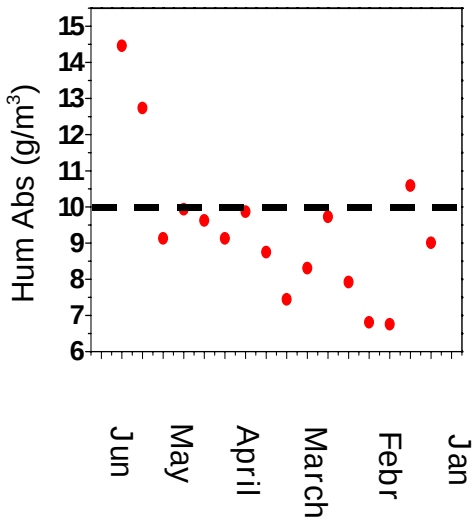

Fig. 3.16: The humidity trend all over the year, measured in our laboratory.

In June the absolute humidity reaches the higher values, which cannot be lowered below $10g/m^3$, even when the room is equipped with a dehumidifier. Some examples of the effects of high absolute humidity values on the morphology of the samples are shown in fig. 3.17.

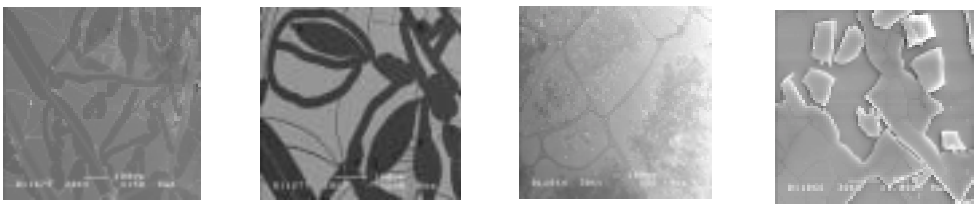

(a) **(b)** **(c)** **(d)**

Fig. 3.17 (a,b,c,d): CeO_2 thin films grown on YSZ single crystals . Due to the high humidity during the deposition process, the films, once grown, present cracks all over the surface.

Fig. 3.17 (a,b,c,d) are SEM images of cerium oxide samples , deposited under a high Abs. Hum. and grown up in standard conditions (see pag.60). In fig.3.17(c,d) it is possible to see both cerium oxide and the underlying YSZ substrate. Another example of how humidity could affect the wettability in CSD deposition is presented in fig. 3.18.

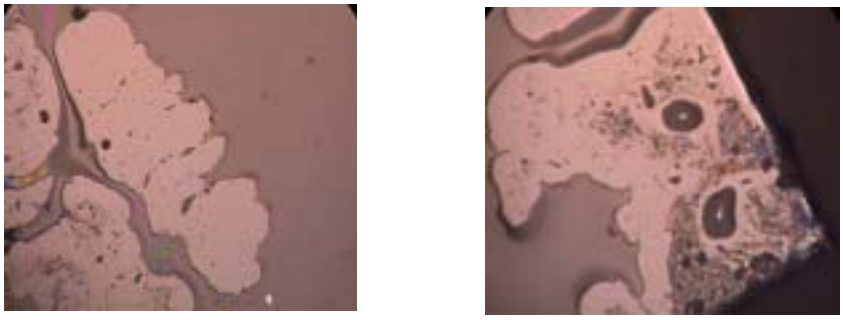

Fig. 3.18: Optical images of a YBCO precursor film just after deposition. The high absolute humidity induces dewetting of the film.

Just a few minutes after a TFA-YBCO solution deposition on a $LaAlO_3$ substrate, an optical microscopy analysis, fig.3.18, has been performed shown how the homogeneous film has surprisingly begun to dewet. The MOD method to prepare CeO_2 is less sensitive to humidity and only after growth the fingerprints of the water action are visible; on the contrary in MOD-TFA is affecting macroscopically the deposited film just before the sample treatment.

Probably when the absolute humidity is too high the substrate, just before deposition, is covered by a film of water. When we drop the precursor solution on the single crystal, the solution and water will mix together and form a non homogeneous film. Depending on the solvent the effect will be more or less important as shown above. Film inhomogeneity makes that some parts of it have different composition and therefore a different surface tension [5] (fig. 3.19).

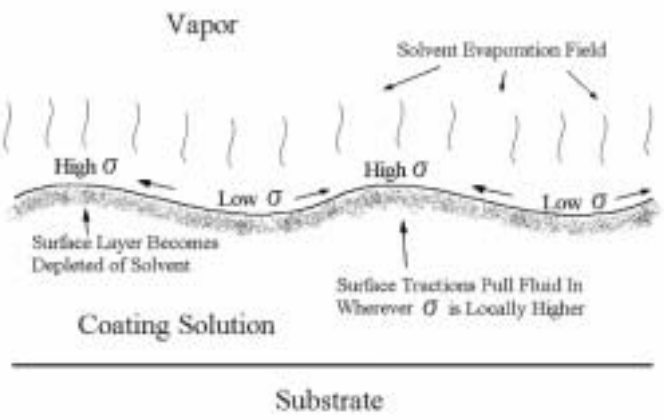

Fig. 3.19: The evaporation process makes the top layer to have a different composition and therefore a different surface tension. The presence of water can increase the differences in surface tension on the sample, causing defects in the film.

Depending on the kind of solvent and on the humidity value, the film defects can manifest themselves in an increased coating roughness, micro cracking of the coating upon further drying, exaggerated striation formation, etc.

A useful way to control the quality of the pyrolisis is its observation by optical microscopy. In general, when the colour of the film is homogeneous as shown in fig. 3.12(b) the quality of the pyrolysis is high enough to proceed with the synthesis step.

3.2.5 FILM THICKNESS

The best way to control the buffer thickness is by changing the precursor solution concentration. To a lower extent, the buffer layer thickness is also affected by the conditions of the solution spinning deposition. The thickness is inversely proportional to the spinning rate, but there is a lower limit which depends on the acceleration rate [6].

Increasing the thickness by reducing the spinning rate, may not be useful, due to the appearance of inhomogeneities in the film. For this reason we fixed deposition conditions to 6000rpm and an of 3000rpm/s .

The studied solution concentration range is 0.08M-0.7M .Since we could not find a relative etchant for CeO_2 on YSZ, in order to create steps of height equal to the layer thickness, we used two alternative techniques. The first one consists of covering one half of the bare substrate surface with scotch tape. After depositing the buffer layer, the scotch tape is removed thus creating a step with height near to be equal to the layer thickness, as illustrated in fig.3.20. Step heights were measured using an optical interferometric method with a Zygo interferometer, (fig. 3.21).

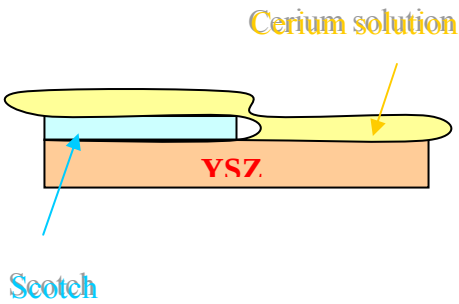

Fig. 3.20 : Sample preparation to measure the CeO_2 buffer layer thickness.

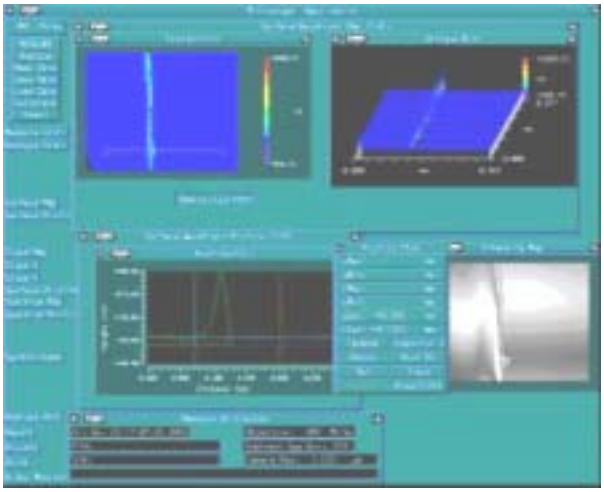

Fig. 3.21: Zygo interferometer. Zygo software permits to obtain a 3D image of the sample analyzing the white light interferences.

Thickness measurements were also performed by X-ray reflectivity (XRR). A typical curve is shown in fig. 3.22. The thickness **d** of the film is given by **d=λ/Δ(2θ)** where Δ(2θ) is angular distance between two consecutive peaks or valleys of the oscillation in the XRR curve (see chapter 1 pag.32).

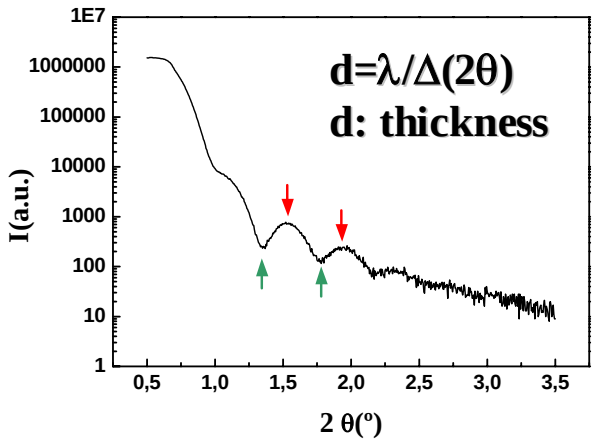

Fig. 3.22: XRR curve. The period of the interference fringes is related to the film thickness

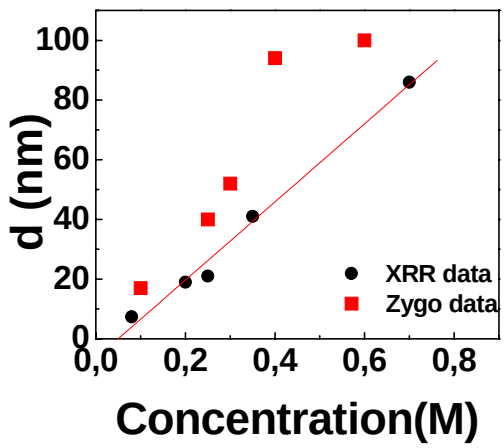

Fig. 3.23 : Dependence of the film thickness with concentration of the Ce precursor solution. In the figure are shown both kinds of data, the red ones by interferometry and the black ones by XRR. The linear fit has been performed using the XRR data.

A clear linear dependence allowing the precise tuning of the layer thickness is observed. Theoretically the thickness depends on the square root of the viscosity. The viscosity directly depends on the concentration of the coating solution [7]. The fit of the data obtained by XRR analysis yields: d=130.9*[Sol]-6.5 (fig. 3.23). The R=0.994 value demonstrates the accuracy of method. For very much diluted solutions, at the same synthesis conditions, the films form islands and this linear relation is no more valid, (see chapter 4 pag.104). The difference between interferometry data and reflectivity data can be easily explained. The sample prepared for the interferometric analysis has been half recovered by a scotch thick several hundred of μm. Therefore the solution drop is not spinned on a flat surface but on one having a step, along which the solution is accumulated thus yielding higher values than those obtained by XRR, (fig. 3.23).

It is worth mentioning that a similar correspondence between thickness and concentration was found in the BZO system, (chapter 5 fig. 5.3 pag.112). The BZO precursor solution is prepared by dissolving barium acetate and zirconium

acetylacetonate in glacial acetic acid. For this sol-gel system, where the precursor solution used has the same concentration (similar viscosity) and using identical deposition parameters as those used for cerium, it is not so surprising to verify that BZO film thickness data lies on the same CeO_2 straight line .

For many CSD processes exist a critical value of thickness upon which cracks form and propagate due to the tensile stress developed during the decrease of the film volume upon evaporation, pyrolysis and densification of the polymerised film. To avoid cracking the precursor solution are limited under a certain concentration to maintain the thickness below the critical value. To build thicker films, usually the deposition and pyrolysis of successive coatings are alternated avoiding the formation of cracks. In chapter 5. an example of the consequences of the critical thickness for a BZO film and the theoretical explication are presented.

3.2.6 INTERDIFFUSION

One important characteristic of a good buffer layer is that it has to protect the YBCO film against interdiffusion with the underlying template. With YSZ(IBAD)/SS substrates, Zr can react with the Ba contained in the YBCO film forming BZO at the interface. Hence it is important to check if the very thin CeO_2 buffer (25 nm) is effective against the diffusion of the Zr. Elemental profiling across the thickness of a CeO_2 buffer on a YSZ single crystal was performed by XPS, (fig.3.24).

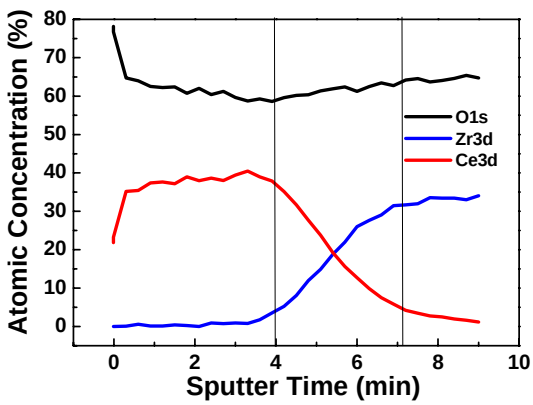

Fig. 3.24: XPS analysis of a 25 nm CeO_2 sample. No relevant interdiffusion between Zr and Ce was found.

The vacuum chamber of the XPS instrument is equipped with an Ar^+ gun, so it is possible to re-sputter the film surface and perform elemental analysis at different film depths. The sputter rate depends on several parameters, and under the conditions employed it is in the range of 3-5 nm a minute. The observed through-thickness distribution of Ce, O and Zr, fig.3.24, reveals that the Zr concentration vanishes within a thickness of about 5nm at the interface, indicating that the thin CeO_2 film can act as an effective barrier against Zr interdiffusion.

3.3 FILM STRUCTURE, TEXTURE AND SURFACE MORPHOLOGY

An XRD pattern of a typical 25-30 nm sample of CeO_2 film grown on a YSZ single crystal at 750ºC in Ar/H_2 for 4h is presented in fig. 3.25.

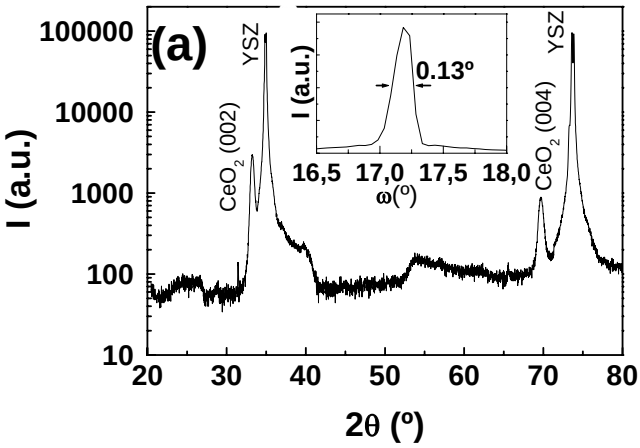

Fig. 3.25: θ/2θ of a CeO_2 film grown on YSZ^{SC} at 750ºC in Ar/H_2 for 4h. (200) rocking curve is shown as inset.

The pattern is presented in a logarithmic scale in order to emphasize the low intensity region. Only (00*l*) peaks are observed, indicating that films with only one orientation were produced. In addition, the pattern reveals that no secondary phases have been formed. The inset shows the corresponding ω-scan taken through the (002) peak, with $\Delta\omega = 0.13º$, indicating an excellent off-plane epitaxial quality.

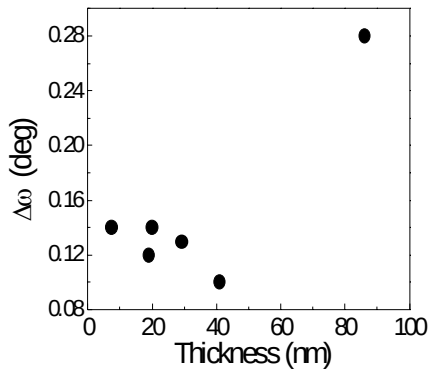

Fig. 3.26: Thickness dependence with the FWHM of (200) rocking curve shows a first decrease of the FWHM until a value of 0.1º for the 41 nm sample. A maximum of 0.28º has been obtained for thicker sample of 86 nm.

The thickness dependence of Δω is presented in fig.3.26. Up to a thickness of 41 nm, Δω values are kept below 0.15°, and a decrease down to 0.1° is observed with increasing thickness. In fact, 0.1º is the value measured for the YSZ substrate, indicating that this is the resolution limit of the diffractometer using parallel beam optics. On the other hand, when the thickness is increased from 41 nm up to 86 nm, the off-plane misorientation spread increases up to 0.28°. Taking into account the polycrystalline nature of the present films, this degradation of the texture quality above a certain "critical" thickness is likely to be associated with the loss of influence of the substrate during the growth process and the accumulation of defects in upper most part of the film.

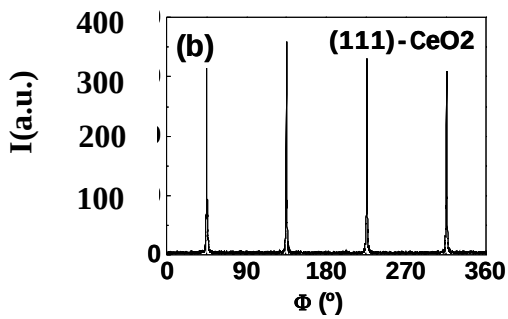

Fig. 3.27: phi-scan of the (111) CeO_2 reflection.

Fig. 3.27 shows a typical (111) ϕ-scan corresponding to a 25-30 nm thick CeO_2 film. The scan shows four peaks 90° apart, thus signalling a unique in-plane orientation.

Moreover, it was verified that the peak positions coincide with those appearing in the ϕ-scan corresponding to the (111) YSZ reflection, thus signalling that CeO_2 grows on (001)-YSZ with a cube-on-cube type epitaxial relationship. In order to ensure that Δϕ is not affected by the neighbouring (111) reflection of the YSZ substrate, θ/2θ scans were recorded through the CeO_2 and YSZ (111) reflections at a sample inclination of χ=54.7°. It was found that the (111) reflections of CeO_2 and YSZ are separated enough in 2θ to ensure that the recorded ϕ-scans are representative of the CeO_2 film texture.

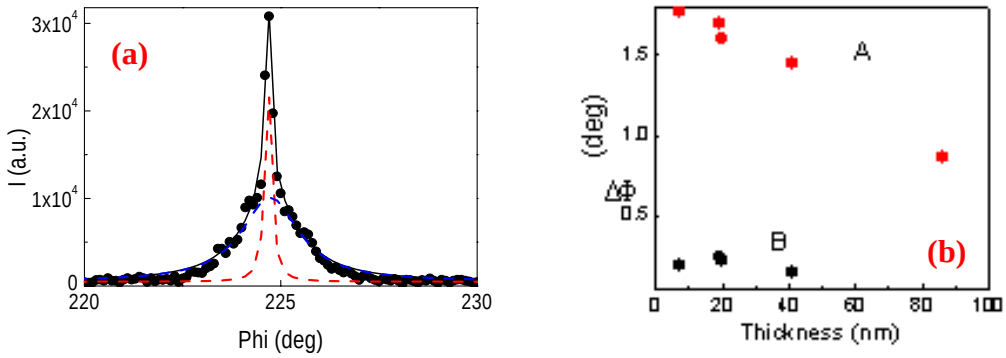

Fig. 3.28(a,b): (a) ϕ scans corresponding to the (111) reflection of CeO_2. Dots correspond to experimental curve and solid line is a least-squares fit assuming two Gaussian contributions, displayed as dashed lines. (b) thickness depends of phi [9].

Careful inspection of the ϕ-scan peaks reveals that the peaks consist of two contributions, fig. 3.28(a), one broad peak and a superposed narrow one, and that their relative weight is thickness dependent [9]. Fig. 3.28(b) is a plot of the FWHM values corresponding to both contributions as a function of film thickness. It can be observed that while the width of the narrow and intense peak is kept constant up to a thickness of 41 nm, the corresponding values for the broad peak decrease with increasing thickness.

At a thickness of 86 nm, the narrow component disappears. The width of this peak follows the slope defined by the broader peaks corresponding to the thinner films. The observed line shape of the ϕ-scans strongly suggests the coexistence of regions with different epitaxial quality. This result, with the preceding ϕ-scan analysis, strongly suggests a bimodal type texture distribution, in which those grains nucleated on the substrate are cube on cube oriented and would be responsible of the narrow component

of the ϕ-scan, while this orientation would be lost towards the surface of the films, generating a widder component.

An average measure of the surface disorder was obtained from RHEED patterns (which are sensitive to the top-most material at the surface). The pattern shown in fig. 3.29 for a typical CeO_2 film grown in Ar/H_2 at 750ºC, clearly reveals diffraction rings consistent with a randomly oriented surface.

Fig 3.29: RHEED pattern of a CeO_2 film grown on YSZ at 750ºC in Ar/H_2 exhibiting diffraction rings characteristic of a randomly oriented surface.

3.3.1 ROUGHNESS VS THICKNESS

The surface roughness of a buffer layer is of primary importance in controlling the quality of the material deposited on it. The flatter is the surface the better will be the texture of the film grown on it [10]. We studied with Atomic Force Microscopy (AFM see chapter 1. pag.35) the surface roughness of different samples of cerium oxide on YSZ deposited from solutions having different concentrations and synthesised at different temperatures.

We investigated concentrations in the range 0.08-0.9M, corresponding to thicknesses between 8 to 90 nm. In fig. 3.30 (a,b), the topographic AFM images of two different samples with thickness d=20 and 90 nm , are shown. It can be observed that the grain sizes which are closely related with the roughness are very similar in the two images. Fig. 3.31 shows a plot of the roughness rms values obtained at different layer thickness from analysis of 20·20 μm areas.

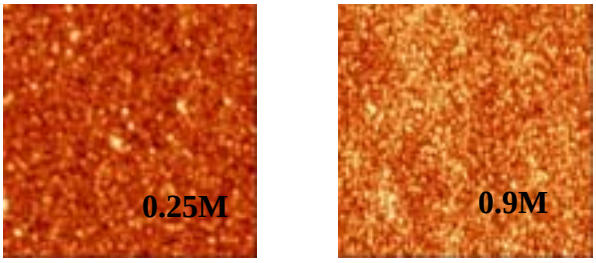

(a) (b)

Fig. 3.30(a,b): CeO_2 film grown on YSZ single crystal. (a) is a 25-30 nm thick film (0.25M), and (b) 90 nm (0.9M).

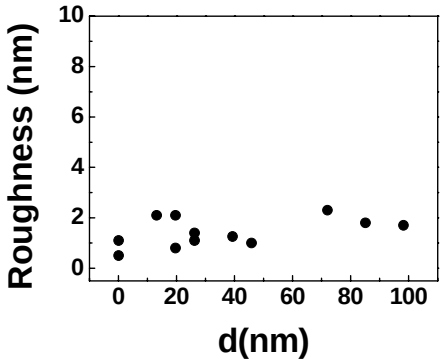

Fig. 3.31: Plot of the CeO_2 surface roughness versus the film thickness .

It is possible to conclude from this plot that the precursor solution concentration, and so the CeO_2 thickness, does not affect the surface roughness. The slight dispersion of the data around a straight line is acceptable considering that the AFM analysis of an area of 20·20 μm may be not representative of the 5·5 mm surface.

3.3.2 ROUGHNESS VS GROWTH TEMPERATURE

To study the temperature effect on roughness, we prepared several 25-30 nm thick layers of CeO_2 on YSZ at temperatures comprised between 650°C and 900°C in an Ar/H_2 atmosphere and with a dwell at $\mathbf{T_{max}}$ fixed in four hours. Typical AFM images obtained at different temperatures are presented in fig. 3.32.

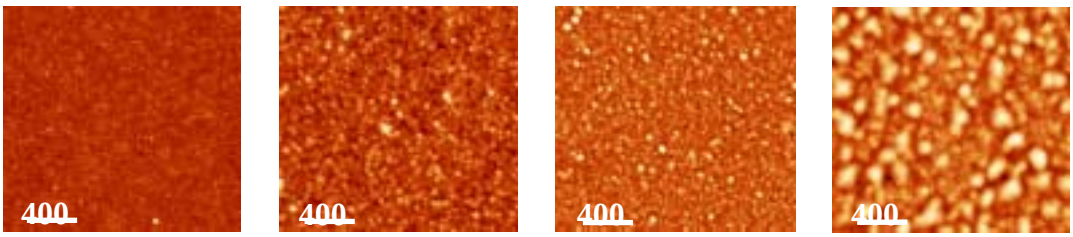

650ºC **750ºC** **800ºC** **900ºC**

Fig. 3.32: 2·2 μm scan AFM images. The CeO_2 samples had been synthesised at the same standard conditions except for the T_{MAX} : 650ºC, 750ºC,800ºC and 900ºC.

The grain sizes increase with the temperature and so does the roughness (fig. 3.33(a,b)). For all the roughness measurements we used a scan area of 20·20μm.

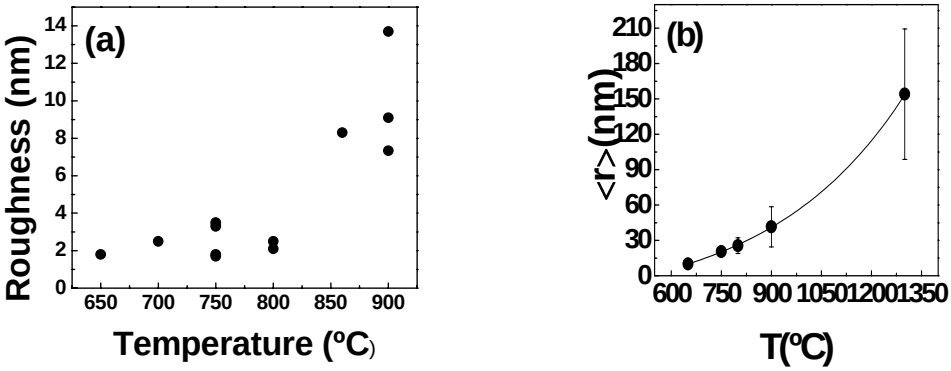

Fig. 3.33(a,b): Plot of the roughness versus synthesis temperature. Roughness (a) and grain size (b) are strictly correlated each other and with the synthesis temperature.

It can be observed that the roughness increases exponentially with temperature. Figs 3.33(a,b) displaying the temperature and thickness dependence of the roughness, respectively are illustrative of the mechanisms governing the roughness evolution in the present films. They clearly reveal that following the same behaviour as the grain size, the roughness increases notably with temperature, while it is not affected by the thickness of the films. Therefore, surface roughness is controlled by grain size effects, which in the present films are not dependent on the thickness as they behave almost as a 3D system.

Also the dwell time at $\mathbf{T_{max}}$ has an effect on the roughness of the cerium oxide buffer layer. Fig. 3.34(a,b) shows a CeO_2 layer of 25-30 nm grown at 1100°C in Ar/H_2 for 15 minutes.

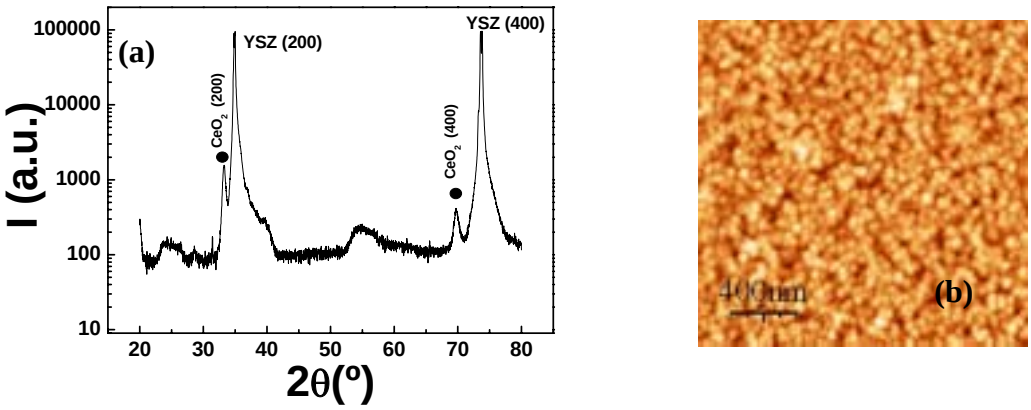

Fig. 3.34(a,b) : (a) the XRD pattern of a sample grown at 1100ºC for 15 min. (b) AFM analysis: the rms roughness value of the film surface is 3.9 nm.

The roughness value we found is less than that expected for a standard dwell time of 4h; 3.9 nm instead of the 8-12nm obtained under the same conditions but with T_{Max} = 900ºC, (see fig. 3.32).

A cross section SEM image of a 100nm thick sample of CeO_2 grown at 900ºC in Ar/H_2 for 4h is presented in fig. 3.35.

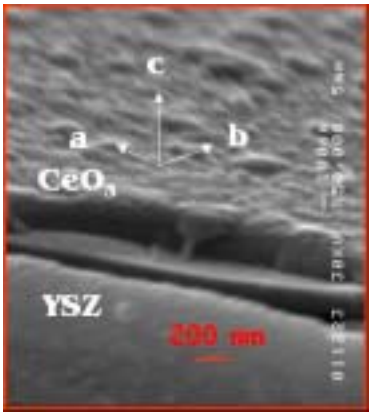

Fig. 3.35: Cross section image of a CeO_2 film on YSZ single crystal.

3.4 CONLUSIONS

The optimisation of precursor solution preparation and the synthesis parameters for CeO_2 thin film growth in Ar/H_2 have been achieved. The optimised process to grow ceria under reducing conditions is reported below:

- 2,4 Ce-acetylacetonate dissolved in acetic acid and stabilized with a 5% in volume of water
- Range of precursor solution concentration (0.2-0.4M)
- Spinner condition:13 µl drop of solution , 6000 rpm at 3000 rpm/s for 2 min.
- Thermal ramp: 60ºC/h till 250ºC a dwell of 30 min, ramp of 200ºC/h till 750ºC and final dwell of 4h. Oven atmosphere Ar/H_2.

The ceria film properties obtained using these synthesis parameters are resumed:

- Controlled roughness value: less than 2nm rms in 20·20μm area scan.
- Apparently high textured samples, ω-scan FWHM=0.1-0.3º and ϕ-scan FWHM=0.2-1.5º
- 25-30 nm CeO_2 films are an effective barrier to the interdiffusion of the substrate as demonstrated by XPS profile analysis.

The complex epitaxial thin film growth of MOD-CeO_2 will be presented in a wide a complete way in the next chapter.

REFERENCES

[1] E.Pretsch, T.Clerc, J.Seibl, W.Simon, *"Tablas para la elucidacion estructural de compuestos organicos por metodos espectroscópicos" Edition Alambra Pag. H370 (1991).*

[2] M.Paranthaman, S.S.Shoup, D.B.Beach, R.K.Williams, and E.D.Specht, Materials Research Bulletin*, **32**, 1697-1704, (1997).*

[3] A.Cavallaro, O.Castaño, A.Palau, J.C.Gonzalez, M.D.Rossell, T.Puig, F.Sandiumenge, N.Mestres, S.Piñol, X. Obradors, *Journal of the European Ceramic Society **24,** 1831-1835 (2004).*

[4] The Aldrich library of FIT-IR spectra , *Edition I, Charles J.Pouchert, vol III, fig 511B.*

[5] http://www.mse.arizona.edu/faculty/birnie/Coatings/Defects.htm

[6] T.Araki, H.Kurosaki, Y.Yamada, I.Hirabayashi, J.Shibada and T.Hirayama, *Supercond. Sci. Technol., **14**, 783 (2001).*

[7] T.Araki, K.Yamagiwa and I.Hirabayashi *Cryogenics, 41, 675 (2001).*

[8] E.S.Putna, T.Bunluesin, X.L.Fan, R.J.Gorte, J.M.Vohs, R.E.Lakis, T.Egami, *Catalysis Today, **50**, 343-352, (1999).*

[9] J. Gàzquez, A. Cavallaro, F. Sandiumenge, O. Castaño, T. Puig and X. Obradors *Supercond. Sci. Technol (to be published).*

[10] J. W. McCamy, D. H. Lowndes, J. D. Budai, R. A. Zuhr, and X. Zhang, J. Appl. Phys. **73**, 7818 (1993).

Chapter 4

GROWTH MODEL FOR MOD-CeO_2

4.1 GROWTH IN AN Ar/H_2 ATMOSPHERE

As reported in the preceding chapter, results of ϕ-scan and RHEED measurements suggest a bimodal misorientation distribution of the polycrystalline films.

To shed light on the way such an anomalous microstructure is generated under these conditions, samples were investigated by TEM [1]. The microstructure and local chemical composition of the samples was characterised by cross sectional transmission electron microscopy (XTEM) using a Jeol 2010 FEG electron microscope operated at 200 kV (point to point resolution 0.19 nm) equipped with a Gatan Image Filter 2000 EELS spectrometer with an energy resolution of 0.8 eV. Thin foils for XTEM observation were prepared by the conventional cutting, gluing and grinding procedures, followed by a final milling step with Ar ions down to perforation. High resolution XTEM images and Fast Fourier transform (FFT) analysis revealed that only those grains nucleated on the substrate exhibit epitaxial orientation. Fig. 4.1 is a high resolution XTEM image viewed along <100>. The image clearly shows porosity in the central part of the film. Inspection of FFT spectra taken across the interface demonstrated a cube on cube epitaxial relationship of those grains nucleated directly on the substrate.

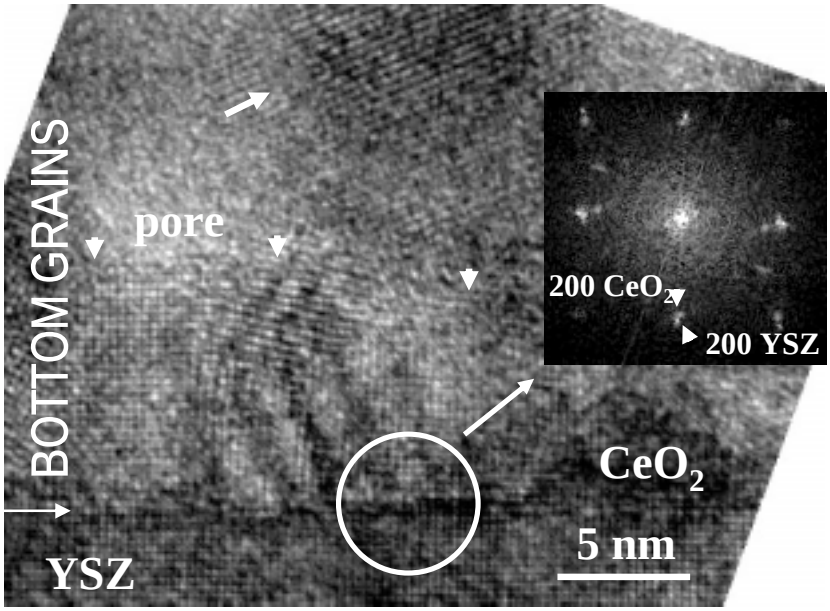

Fig. 4.1: XTEM micrograph of an as-grown CeO_2/YSZ film viewed along the <100> direction, showing a nanometric granular and porous microstructure. Interface is indicated by an horizontal arrow. Inset shows the FFT spectrum taken across the interface, including CeO_2 crystallites nucleated on the substrate (indicated by arrowheads), demonstrating their cube on cube epitaxial relationship. Thicker arrow indicates a grain nucleated ahead of the substrate interface. By inspection of lattice fringes it can be deduced that it is misoriented relative to the first layer of epitaxial crystallites [2].

Conversely, the effect of the substrate is rapidly lost with distance from the interface. Fig. 4.2 is a high resolution XTEM image of grains located at the surface of the film. Inspection of lattice fringes clearly reveals strong misorientations between grains, in agreement with the REED measurements reported in the preceding chapter.

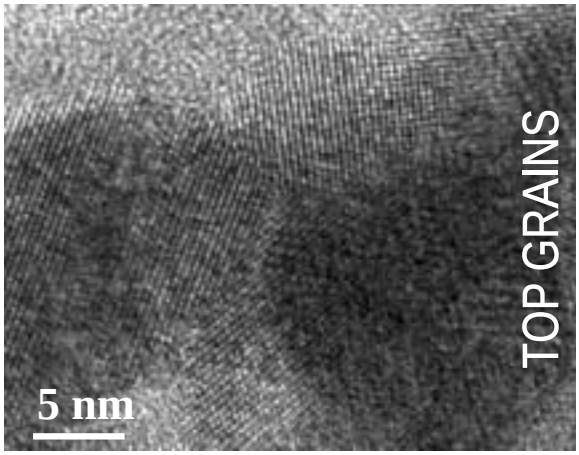

Fig. 4.2: High resolution XTEM image showing a detail of the grain structure at the top-most region of the ceria film grown in Ar/H_2 [2].

Since the ceria melting temperature is near 2400ºC, and nucleation happens at 500ºC, (F.Barberich, private communication), the undercooling is large enough to induce homogeneous and heterogeneous nucleation with almost equal probabilities.

TEM images in fact, typically show a nanometric granular and porous microstructure which contrasts with the columnar microstructure usually reported for films deposited by vacuum techniques, or even the dense microstructure achieved in other CSD derived oxide films [3]. Grains are rounded with size typically comprised between 5 and 10 nm, and no significant through-thickness grain size variations are observed. AFM images (chapter 3 pag.72) exhibit a granular morphology also consistent with XTEM imaging (fig. 4.2).

4.2 POST ANNEALING IN STATIC AIR ATMOSPHERE

As reported by J.C. Nie [4] on CeO_2 by PLD (Pulsed Laser Deposition), an annealing in oxygen has the effect of making the cerium surface smoother. We tested different post annealings, in oxygen or static air, at 1300ºC, 1000°C, and 900ºC, for 4 hours, and the sample roughness was much lower that that achieved at the same temperature but in Ar/H_2 atmosphere. The effect of oxygen post annealing is shown in fig.4.3(a,b).

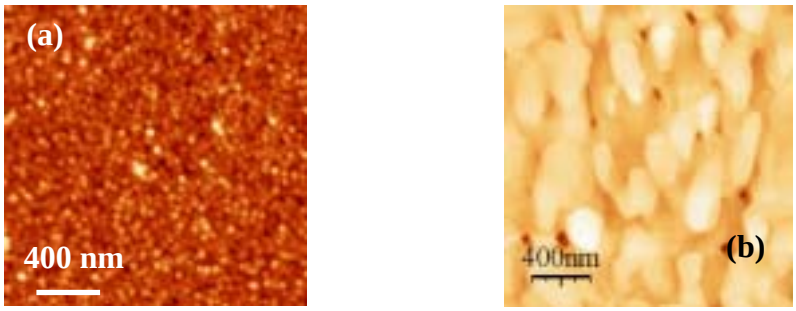

Fig. 4.3(a,b) : (a) AFM image of a standard sample of 25-30 nm thick CeO_2 grown at 750ºC for 4 hours. (b) is the same sample but after a post annealing at 1000ºC in static air[5].

AFM topographic images reveal that the granular surface has evolved to a terraced one (fig. 4.3(a,b)). It is evident the complete reconstruction in the surface morphology of the ceria thin film.

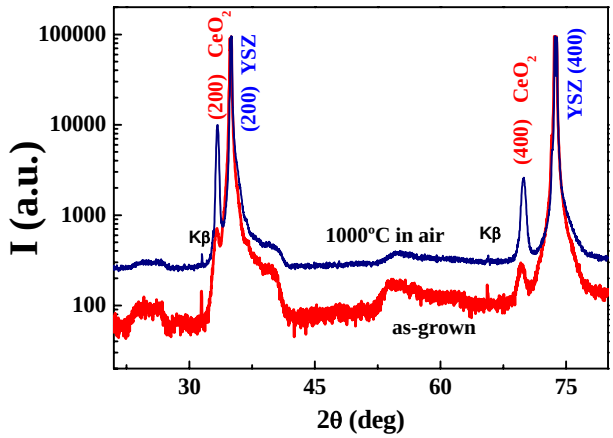

Fig. 4.4: The red XRD pattern corresponds to a sample grown in standard conditions at 750ºC. The deep blue pattern corresponds to the same sample after the annealing at 1000ºC in static air [5].

Fig. 4.4 compares the XRD spectra of a sample before and after annealing in static air. It is clear that the intensity of the (h00) peaks of the CeO_2 significantly increase in the case of the oxygen annealed sample, indicating an unexpected enhancement of the crystallinity of the film.

In PLD CeO_2 samples, the material is completely oriented (00L) and the oxygen has only the effect of obtaining a flatter surface [4]. Our sample instead, after synthesis in Ar/H_2, show epitaxial grains only at interface substrate-film, and the annealing has also the effect of re-orienting the disordered part of the film.

Fig. 4.5(a) is a low magnification XTEM image of a film post-processed at 1000ºC in static air. Clearly, the granular microstructure has evolved to an epitaxial single crystalline film thus explaining the increase in intensity of the (00l) peaks (fig. 4.4). Unexpectedly, the images show that at variance with as-grown films, here the surface has developed a terraced topography terminated by (001) planes, in agreement with the AFM image shown in fig. 4.3(b).

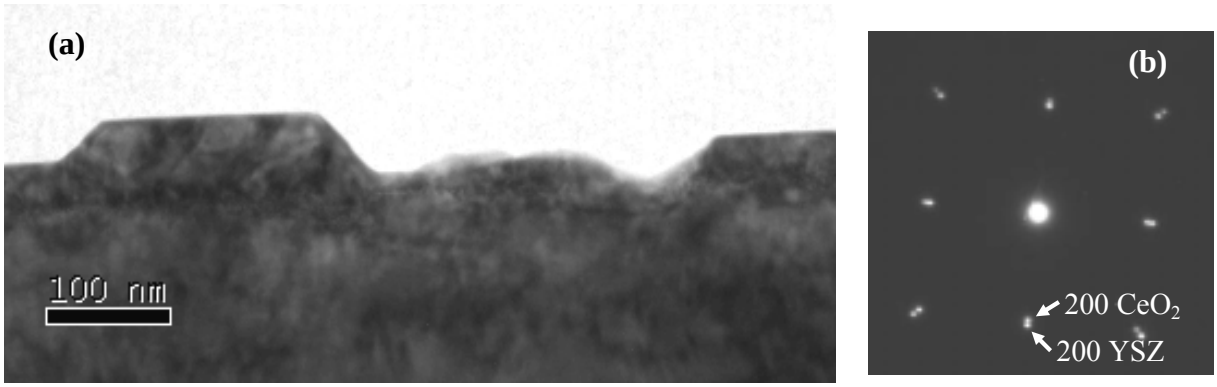

Fig. 4.5(a,b): Low magnification XTEM micrograph of a CeO_2/YSZ film post-processed at 1000ºC under oxidising conditions, viewed along the <100> direction. (a). Corresponding SAD pattern (b) [2].

Fig. 4.5(b) is a characteristic [100] SAD pattern that includes YSZ, demonstrating the cube on cube epitaxial relationship between the whole film and the substrate.

Fig. 4.6(a) is a high resolution XTEM image revealing a patched like contrast distribution baring witness of the granular precursor microstructure. Fig. 4.6 (b) is a FFT filtered image of the same area emphasising the defect structure. Such contrast behaviour was typically found in high resolution images taken throughout the film and suggests that a higher degree of crystallographic coherency can be achieved upon longer annealing steps. The images also make evident the development of an evenly spaced array of misfit dislocations, encircled in fig. 4.6 (b).

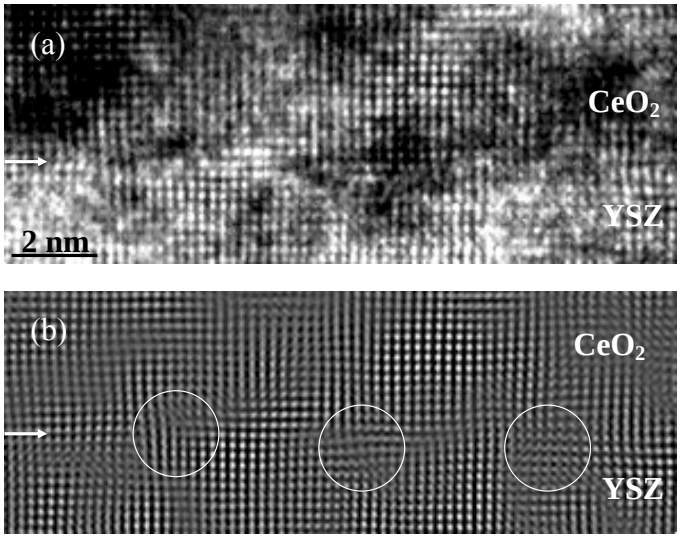

Fig. 4.6(a,b): High resolution image of the interface of a film submitted to post-processing under oxidising conditions viewed along the <100> direction (a), and corresponding Fourier filtered image emphasizing the patched like contrast and array of interfacial dislocations, enclosed by circles (b) [2].

An accurate analysis of the structure of the misfit dislocations is beyond the scope of the present work. However, according to the fluorite structure of both film and substrate, their Burgers vector is likely to be of the type b=1/2<110>. The development of a misfit dislocation array is consistent with the slight, though significant decrease of the residual stress, σ, determined for this post-processed film [1].

Fig. 4.7 is an AFM image exhibiting a (001) terraced surface in accordance with the XTEM image shown in fig. 4.5(a). The (001) terraces are very flat as indicate by the AFM profiles; there lengths are in a range of 100-300 nm as confirmed by TEM.

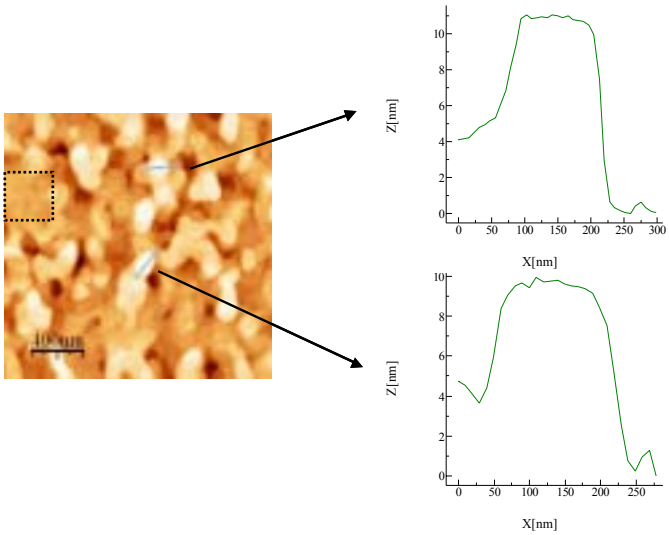

Fig. 4.7: AFM analysis of CeO_2/YSZ sample post annealed in static air at 1000ºC exhibits a terraced surface in agreement with XTEM images [5].

The rms roughness for the 20·20μm area scan is 3.2 nm is similar to that corresponding to the as-grown films, but locally, as e.g. within the area under the black square, in fig. 4.7 it is possible to obtain rms values under 1nm. The AFM image of fig. 4.7 evidences a homogeneous distribution of the facetted hillocks. Such hillocks result from a sintering process involving an intense reorientation and faceting of top most grains in as-grown films. Hence, further improvement of surface roughness deserves further investigation of these mechanisms.

A RHEED pattern of a sample post annealed at 1300ºC in static air, see fig. 4.8, reveals a crystallographically ordered surface.

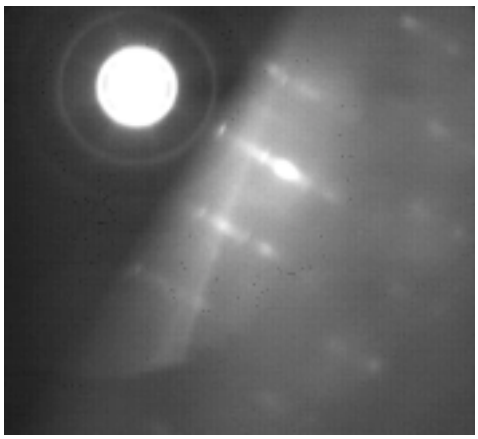

Fig. 4.8: RHEED pattern of a CeO_2 samples grown in standard condition, and post annealed at 1300ºC in static air. The RHEED image exhibits a spot-like pattern indicating an ordered surface [5].

After many experiments of ceria reconstruction by post annealing, we associated the success of the air treatment to the evolution of the granular microstructure to an epitaxial one. The AFM surface analysis (apparition of (001) terrace morphology) and the increase of the (00L) peak till a maximum value (~10000 a.u.), constitute useful finger prints of the epitaxial re-orientation of the film. More experiments are going on to verify if similar effects are observed at lower temperatures than 900°C.

The evolution of crystallinity was monitored through the intensity of the (200) peak of ceria. Several experiments to reproduce these results on the ceria thin films by post annealing have been performed. The samples were all prepared with a 0.25M precursor solution, synthesized at 750ºC for 4h in Ar/H_2, and post oxidised at 1000ºC in static air. It was found that the maximum intensity of the CeO_2 peak is always correlated with the appearance of the (001) terraced morphology.

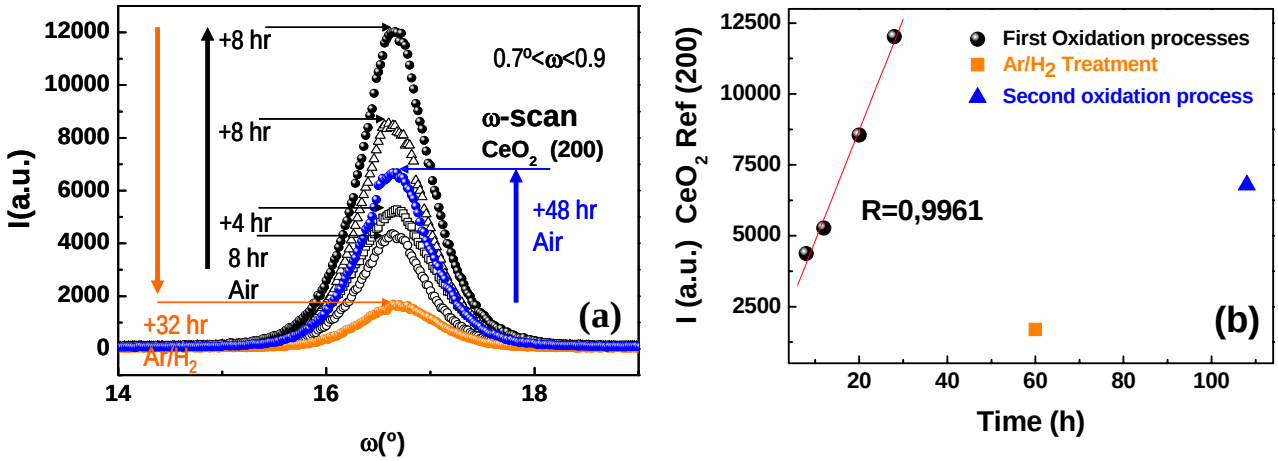

Fig. 4.9(a,b): Rocking curves around the (200) reflection of CeO_2 films submitted to various treatments. The (200) peak of cerium oxide increases its intensity until a maximum by following annealing in static air at 1000ºC. Once reached the maximum peak intensity, the film it is completely epitaxial; annealed under reductioning conditions its microstructure changes again and the intensity decreases, (orange curve). This process is reversible as demonstrated by the last annealing in air, blue curve (a). The CeO_2 intensity exhibits a linear dependence with the annealing time in static air (b).

In fig. 4.9(a) is presented a sample treated in air at 1000ºC in several steps up to 30 hours until the ceria film has been completely reoriented to (00l). After each treatment we analysed the sample by XRD. The successive treatments were in order: 8h, 4h, 8h, 8h. The (200) peak of CeO_2 increases gradually till a maximum intensity (~12000 a.u.) after 28 hours in air. This increase follows a linear dependence with oxidation time as proved by the small R value, R=0.996, (fig. 4.9(b)). Subsequently we submit the film completely textured for 32 hour in a reducing atmosphere (Ar/H_2 at 1000ºC); the material loses its texture, the (200) peak decreases below 2000 counts (orange curve). Strikingly the reorientation of the ceria thin films appears to be a reversible process, as indicated by the increase in intensity in the last sixth treatment in oxygen, 48h, (fig.4.9(a,b)). Depending on the atmosphere, Ar/H_2 or air, the random orientation or the epitaxial one is preferred.

It is well known that ceria has Ox/Rid properties useful in different applications as in catalyst [6,7] or in fuel cell [8,9] technology. To confirm that this CeO_2 Ox/Rid behaviour is independent of the synthesis technique, we annealed a 75nm of sputtered ceria on YSZ produced by Cryoelectra, in Ar/H_2 atmosphere. In fig. 4.10 XRD the ω-scan analysis after 24 and 48 hours of treatment shows a decrease of the intensity of the (200) peak due to a loose of texture of the sputtered CeO_2-film.

Again, it is found that the process is reversible, and a final post-annealing in air (50h) increases the value to the initial maximum intensity (~20000 a.u.).

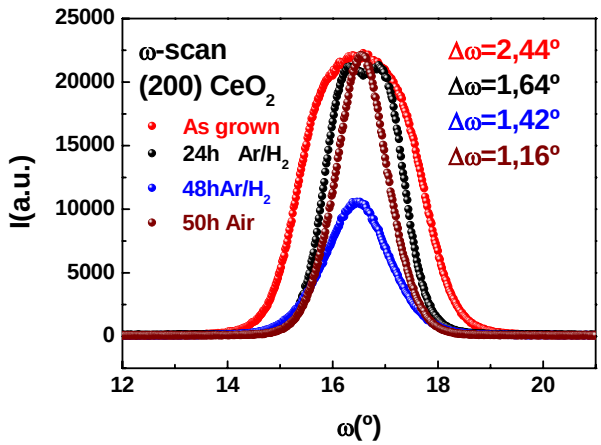

Fig. 4.10: A film of sputtered-CeO_2 film annealed in Ar/H_2 for 72h and then for 50h in static air, presents the same reversibility behaviour of the microstructure transformation found for the MOD- CeO_2 film.

In order to investigate the influence of the oxidation state of Ce ions on the microstructure, we compared the XPS spectra of as grown and processed samples. XPS analysis of a sample synthesised in standard conditions and one of a post annealed sample in static air are presented in fig.4.11(a,b).

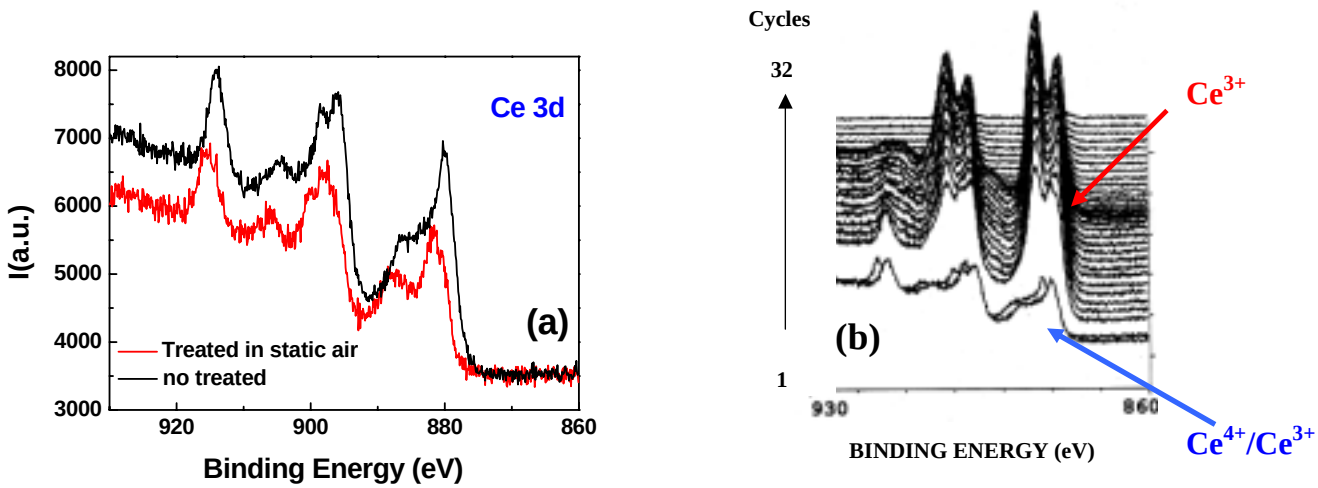

Fig. 4.11(a,b): (a) Surface measurements of two samples; one synthesized in Ar/H_2 (black line), and the second submitted to a post annealing in static air (red line). (b)The apparatus alternates a XPS measure with a re-sputtering of the sample surface. Cycle 1 is an analysis of the surface, cycle 32 is already a measure of the single crystal, the 3d Ce signal has disappeared.

XPS is a very sensitive surface technique, chapter 1 pag.34, and permits to know the oxidation state of cerium. In these systems, Ce^{3+} and Ce^{4+} species can be distinguished because of the distinct shapes of their respective Ce3d signals [10-13].

Owing to a complex shape of the Ce3d spectra it is very difficult to quantify the percentage of each species. Nevertheless in fig. 4.11(a), the peak at 885 eV better defined for the sample treated in air (red line), suggests a higher quantity of Ce IV respect to Ce III [14].

Fig. 4.11(b) shows an XPS through–thickness Ar^+ milling analysis of a sample grown in Ar/H_2. The profile of the Ce3d spectra with the ceria thickness indicates a large amount of Ce III. Unfortunately this is only an effect due to the reduction of the Ce IV by the Ar^+ as reported by J.P.Holgado et al. [15]. It is therefore impossible to follow the evolution of the oxygenation state of cerium across the thickness of the film by Ar^+ milling.

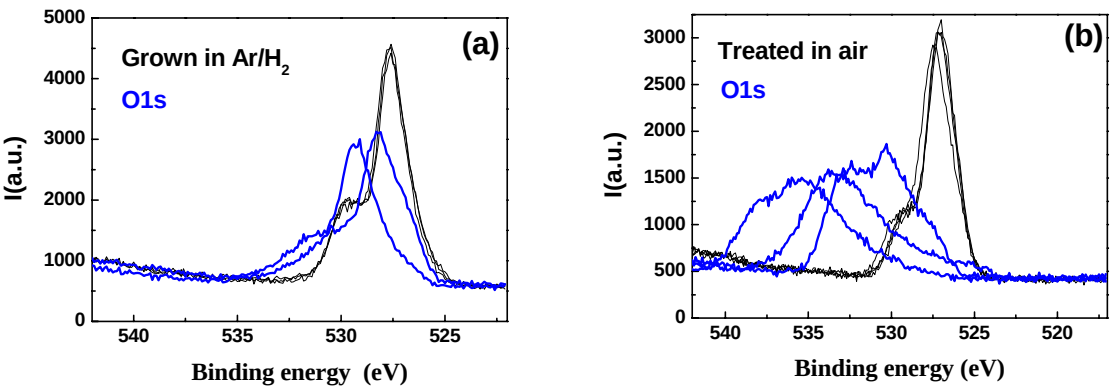

Fig. 4.12(a,b): XPS analysis of the O 1s spectra measured for a ceria sample just after growth in Ar/H_2 (a), and of a post annealed one in static air (b). Blue curves are the measurements of the film surfaces while the black ones have been achieved after Ar+ milling.

A shoulder in the O1s spectra appears with the increase of the reduction state of the ceria film, (fig. 4.12(a,b)) [15]. The blue lines are measurements taken before re-sputtering with Ar^+, the black ones are after the attack, (fig. 4.12(a,b)). Also this spectrum confirms that the amount of Ce III is higher in the as grown sample than in the annealed one, as indeed expected. Different masking effects difficult the exactly quantification of the reduction percentage of CeO_2 in the films [15], and include an investigation of the distribution of Ce^{III}/Ce^{IV} across the thickness of the films.